PHYSICAL REVIEW D VOLUME 25, NUMBER 3 1 FEBRUARY 1982

Measurement of the magnetic moment of the positive muon by a stroboscopic muon-spin-rotation technique

E. Klempt, R. Schulze,* and H. Wolf
Institut für Physik der Universität Mainz, D-6500 Mainz, Federal Republic of Germany

M. Camani,* F. N. Gygax, W. Rüegg, A. Schenck, and H. Schilling
Laboratorium für Hochenergiephysik der Eidgenössichen Technischen Hochschule Zürich, c/o Schweizerisches Institut für Nuklearforschung, CH-5234 Villigen, Switzerland

(Received 30 March 1981)

A new determination of the magnetic moment of the positive muon in units of the magnetic moment of the proton is presented. The Larmor precession of positive muons in liquid bromine was observed by a stroboscopic technique in a field of 0.75 T and combined with concomitant proton NMR measurements in the same chemical environment. The stroboscopic method allows use of the full muon stopping rate available at the Schweizerisches Institut für Nuklearforschung (SIN) muon channel. Moreover, it permits an intrinsically precise determination of muon Larmor frequency and proton NMR frequency measuring the magnetic field by comparison with the stable reference frequency of the SIN accelerator ($\Delta\Omega/\Omega \approx 10^{-8}$). Two different bromine targets were used which allowed an unambiguous determination of the chemical field shift experienced by the muons. One target contained pure and water-free liquid bromine (Br_2), where stopped muons form (μ^+e^-)Br molecules. The other target was slightly contaminated with water; there a chemical reaction chain places the muons into (μ^+e^-)HO molecules. The diamagnetic shielding of protons in the analogous molecules HBr and H_2O in liquid bromine was measured by high-resolution NMR. Values for the isotopic shift of the diamagnetic shielding, when protons are replaced by muons, are available from quantum chemical calculations. After application of the chemical-shift corrections, the results from the two different bromine targets are consistent. The final result is $\mu_\mu/\mu_p = 3.183\,344\,1(17)$ (or ± 0.53 ppm). This value agrees with other recent precision determinations of μ_μ/μ_p. For the muon mass the present result implies $m_\mu/m_e = 206.768\,35(11)$ (± 0.53 ppm).

I. INTRODUCTION

This paper reports on a sub-ppm determination of the muon magnetic moment in units of the proton magnetic moment, μ_μ/μ_p. The magnetic moment of the positive muon is derived from a measurement of the Larmor precession frequency of muons stopped in a liquid bromine target. The experimental method exploits the time structure of the accelerated proton beam (~50 MHz) of the Schweizerisches Institut für Nuklearforschung (SIN) by means of a stroboscopic technique in order to allow use of the full beam intensity.

Results of a preliminary analysis of the data have already been communicated[1]; here we present a full discussion of the stroboscopic method—particularly of its applicability to a high-precision experiment—and of the data analysis. Furthermore, we discuss in detail the chemical processes involved when muons are brought to rest in liquid bromine and the resulting diamagnetic shielding of the external magnetic field. We show that in liquid bromine only one molecular species containing muons is formed (MuBr, or MuHO if a small water contamination is added to the bromine target; Mu = μ^+e^- = muonium), and that the diamagnetic shielding of muons in these molecular compounds can be determined by a combination of proton NMR studies and quantum-theoretical first-principles calculations. This is to be contrasted to the situation in water, where the poor knowledge of the isotope effect of the diamagnetic shielding had limited the final accuracy in previous determinations of μ_μ/μ_p.[2]

At the time when this experiment was initiated, three precision experiments on the muon magnetic moment had been performed:

(i) From the measurement of Zeeman transition frequencies in muonium in a gaseous target in a strong magnetic field, a value of

$$\mu_\mu/\mu_p = 3.183\,349\,0(150),\ 4.8\ \text{ppm}$$

was derived.[3] This value included a theoretical pressure-shift correction of 7.8 ± 2.3 ppm.

(ii) By observation of the precession frequency of muons stopped in H_2O and $CH_2(CN)_2$, μ_μ/μ_p was determined to[2]

$$\mu_\mu/\mu_p = 3.183\,346\,7(82),\ 2.6\ \text{ppm}.$$

The dominant part of the error arose from the unknown isotope effect of the diamagnetic shielding.

(iii) Finally, the muon magnetic moment is related to the hyperfine-structure (HFS) separation of muonium by means of the formula

$$\nu_{\mathrm{HFS}} = \tfrac{16}{3}\,\alpha^2(\mu_\mu/\mu_p)(\mu_p/\mu_B)R_\infty c(1+\text{QED corrections}). \quad (1.1)$$

The fine-structure constant, the Rydberg, and the proton magnetic moment in unit of Bohr magnetons were known with errors well below the 1-ppm level. Under the assumption that uncalculated higher-order contributions to the QED corrections were less than 0.6 ppm, a value of

$$\mu_\mu/\mu_p = 3.183\,329\,9(25),\ 0.8\ \text{ppm}$$

was deduced from the measured muonium hyperfine frequency.[4]

This last value differed by 5.4 ppm from the average of the two preceeding direct determinations of μ_μ/μ_p.

In view of this serious discrepancy, a new and more precise experiment was designed to measure μ_μ/μ_p directly by observation of the respective Larmor frequencies in the same magnetic field. Its outcome should help to answer the question concerning the need of considerable corrections to the accepted value of the muonic magnetic moment on the one hand, or the correctness of the QED treatment of the muonium hyperfine splitting on the other. A precise knowledge of μ_μ/μ_p was also of importance for the interpretation of the muon $g-2$ experiment.[5]

In the meantime the QED corrections to the muonium hyperfine frequency were recalculated[6] and higher-order terms were found to contribute significantly to the hyperfine frequency.[7,8] Furthermore, the result of the present work and of another high-precision experiment[9] leads to a complete reconciliation of the above-mentioned inconsistency.

II. THE STROBOSCOPIC METHOD

A. General description

The fundamental principle of the stroboscopic method used in this experiment rests on the microscopic burst structure of the SIN muon beam. Due to its rf acceleration, the primary proton beam has a bunch structure. Under suitable selection of the momenta of pion and muon beam, the muon beam still reflects this bunch structure, and it arrives in sequential burst with about 20-nsec time separation. The time separation is determined by the proton acceleration frequency Ω with $\Omega/2\pi = 50.633$ MHz (see Fig. 1).

The muon beam is polarized; if it is stopped in a transverse magnetic field, individual muons precess at their Larmor precession frequency ω_μ. But as polarization is added into the target at the beam-burst repetition frequency Ω, the polarization of the muon ensemble must be periodic in Ω. A finite polarization of the muon ensemble therefore only builds up if the Larmor precession frequency coincides—at least within the uncertainty relation imposed by the muon life time τ_μ—with the beam-burst repetition frequency or one of its harmonics, i.e., only if $|\omega_\mu - m\Omega| \lesssim 1/\tau_\mu$. If, on the contrary, Larmor precession frequency and beam-burst repetition frequency are mismatched, if $|\omega_\mu - m\Omega| \gg 1/\tau_\mu$, nearly no polarization builds up and the decay asymmetry of the muon ensemble is grossly suppressed.

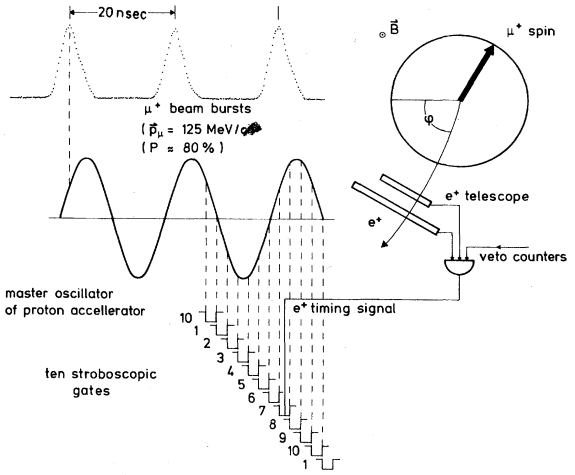

FIG. 1. Schematic representation of the stroboscopic measurement. The incoming, polarized, positive muons are bunched in periodic bursts at the master frequency of the proton accelerator. Their spins precess then in the magnetic field $\vec{B}$. If the Larmor precession frequency is close to a harmonic of the accelerator frequency, the coherently precessing muon ensemble will show a nonvanishing precessing polarization. This is monitored by the decay positrons, which are detected by a counter telescope. The registered counts, vetoed by disturbing background events, are binned into 10 stroboscopic time gates, phase locked to the master accelerator frequency, covering exactly one beam-burst repetition period.

The polarization of the muon ensemble can be observed by a stroboscopic technique, where positrons from muon decay are counted in a suitably gated positron telescope located in the plane of precession. The positron gate is periodic in time, phase-locked to the master oscillator driving the proton acceleration cavities, i.e., to the beam-burst structure. Thus the positron telescope detects size and phase of the muon polarization in a coordinate system rotating at Ω. The positron gate therefore corresponds to a fixed-frequency stroboscopic flash light; the magnetic field has to be scanned in order to find one of those muon-spin-precession frequencies where the fixed-frequency stroboscope detects a stationary polarization.

Of course, several gates can simultaneously be applied to one positron telescope so that positron events are not lost because of the gating. A posi-

tron event detected in the telescope can then be binned into one of the stroboscopic gates. In this experiment ten gates were used. In Fig. 1 the first gate is phase locked to the zero crossing of the rf voltage of the proton accelerator. One rf period is covered exactly by the set of ten contiguous nonoverlapping gates.

A stroboscopic method based on a periodic beam modulation had first been applied by Christiansen *et al.* in a $\gamma\gamma$ perturbed angular-correlation experiment.[10] It was not known whether the method was suited for a high-precision experiment. Therefore we will discuss in detail the line-shape theory of a stroboscopic resonance, but in order to facilitate the reading of this paper, the rigorous derivation is deferred to the Appendix. Here we present only the results of this analysis and show that the stroboscopic method has an intrinsic accuracy exceeding the needs of the experiment. The influence of practical imperfections of our experimental setup on the observed line shape is discussed in conjunction with the data analysis.

B. Stroboscopic signal

Consider a beam of polarized muons which are stopped in a magnetic field. The muon polarization, transverse to the magnetic field, is A'. The incoming muon beam exhibits a periodic time structure of frequency $\Omega = 2\pi/T$. Therefore, the muon stopping rate $B(t)$ is modulated as well and satisfies $B(t) = B(t+nT)$. Positrons emitted in the decay of muons are detected in the positron telescope covering a finite solid angle centered at the angle ϕ, in the plane of precession. The telescope is gated by the electronically defined gate functions $G_j(t)$, which are periodic in time and phase locked to the master oscillator of frequency Ω. We will assume that N stroboscopic gates are constructed and that they are contiguous and do not overlap, so that every positron detected in the telescope falls exactly into one of the gates $G_j(t)$, $j = 1, \ldots, N$. We now ask for the total number of positron counts in the gate $G_j(t)$ during the time interval (t_i, t_f), as a function of the magnetic field or as a function of the muon-spin-precession frequency ω_μ, respectively. The decay probability of a muon stopped at the time t_s in the target is given by $(1/\tau_\mu)e^{-(t-t_s)/\tau_\mu}$. If the decay of polarized muons into the direction Φ' is considered, the expression has to be multiplied by the factor $1 + A' \cos[\omega_\mu(t - t_s) - \Phi']$, $t \geq t_s$. In order to calculate the number of counts N_j in the stroboscopic gate $G_j(t)$, the decay probability has to be integrated over the finite solid angle for detection of positrons in the telescope, over all beam particles which have entered the target and did not yet decay, and over the time in which the stroboscopic gate $G_j(t)$ is active during the data-taking time interval (t_i, t_f). Therefore

$$N_j = \int_{t_i}^{t_f} dt\, G_j(t) \int_{-\infty}^{t} dt_s B(t_s) \int_0^{2\pi} d\Phi' D'(\Phi') \frac{1}{\tau} e^{-(t-t_s)/\tau_\mu} \{1 + A' \cos[\omega_\mu(t - t_s) - \Phi']\}. \tag{2.1}$$

$D'(\Phi')$ is the geometrical detection efficiency as a function of Φ'. The integration over Φ' leads to an average geometrical detection efficiency D,

$$D = \int_0^{2\pi} d\Phi' D'(\Phi'). \tag{2.2}$$

The average decay asymmetry A, as observed by the positron telescope, is defined by

$$AD \cos(\alpha - \Phi) = \int_0^{2\pi} d\Phi' A' D'(\Phi') \cos(\alpha - \Phi'). \tag{2.3}$$

Changing the variable t_s to $t' = t - t_s$ leads to

$$N_j = D \int_0^{\infty} dt' \frac{1}{\tau_\mu} e^{-t'/\tau_\mu} [1 + A \cos(\omega_\mu t' - \Phi)] \times \int_{t_i}^{t_f} dt\, B(t - t') G_j(t). \tag{2.4}$$

The evaluation of this integral is presented in the Appendix. It shows a resonant behavior whenever the muon-spin-precession frequency crosses one of the harmonics of the beam-burst repetition frequency. N_j is given by (A17),

$$N_j = N_0 \lambda_j \left[1 + \sum_{m=-\infty}^{\infty} A_{\text{eff},j}(m\Omega) \frac{\cos\psi_{m,j} - x_m \sin\psi_{m,j}}{1 + x_m^2}\right] \tag{2.5}$$

where N_0 is the total number of positrons detected in the positron telescope and λ_j is the fractional width of the gate $G_j(t)$. $\psi_{m,j}$ is the phase of that gate, defined in the Appendix, and $A_{\text{eff},j}(m\Omega)$ is the effective asymmetry of the corresponding resonance pattern. For Gaussian beam bursts, individually described by

$$b(t) = (\kappa T \sqrt{\pi})^{-1} \exp[-(t/\kappa T)^2], \tag{2.6}$$

the effective asymmetry is determined to be (A18)

$$A_{\text{eff},j}(m\Omega) = e^{-(m\pi\kappa)^2} \frac{\sin(m\pi\lambda_j)}{m\pi\lambda_j} A. \tag{2.7}$$

The dependence on the magnetic field is hidden in x_m, which parametrizes the deviation of the muon precession frequency from the resonance condition:

$$x_m = (\omega_\mu - m\Omega)\tau_\mu \,. \tag{2.8}$$

In the proximity of a resonance $x_m \lesssim 1 \ll \Omega\tau_\mu$, the summation over m in Eq. (2.5) yields only one dominant contribution.

In the experiment ω_μ is controlled by the magnetic field, which itself is determined from the proton spin resonance frequency ω_p; i.e., one may write $\omega_\mu = (\omega_\mu/\omega_p)\omega_p$, where ω_μ/ω_p is proportional to μ_μ/μ_p, as is shown in Sec. II C. It should be pointed out that the stroboscopic technique does not require a measurement of time intervals, but implies the determination of a frequency ratio.

C. Local magnetic fields at the muon and proton sites

The actual magnetic fields at the muon site and at the proton site, respectively, are slightly different from the applied external field B_{ext}, depending on the chemical environments and macroscopic demagnetization effects. The local field at the muon or proton site can be written as

$$B_{\text{loc}} = B_{\text{ext}} - \sigma B_{\text{ext}} - NM + \frac{4\pi}{3} M$$

$$= B_{\text{ext}}\left[1 - \sigma - \left(N - \frac{4\pi}{3}\right)\chi\right].$$

σ is the diamagnetic shielding constant for the muon (or proton) in its particular chemical compound inside the sample, M is the induced bulk magnetization and χ is the corresponding bulk susceptibility of the sample substance, and N is the demagnetization factor, depending on the shape of the sample. The last two contributions to B_{loc} are the demagnetization field and the Lorentz field, respectively.

The proton NMR frequency ω_p measuring the field is obtained from a water probe, thus:

$$\frac{\omega_\mu}{\omega_p} = \frac{\mu_\mu}{\mu_p} \frac{1 - \sigma_{\mu^+} - (N_{\text{target}} - 4\pi/3)\chi_{\text{target}}}{1 - \sigma_{H_2O} - (N_{\text{NMR}} - 4\pi/3)\chi_{H_2O}} \,. \tag{2.9}$$

Diamagnetic shieldings (i.e., chemical shifts) and demagnetization effects will be accounted for by the use of this formula (details in Secs. III and V).

D. Discussion of systematic effects

The stroboscopic line-shape theory leading to Eq. (2.5) has been derived without any knowledge of the structure of the beam bursts or of the stroboscopic gates. It has only been assumed that beam bursts and gates are periodic in time and are derived from the same frequency. The experimental data will, however, be fitted assuming that only one resonance contributes and that the influence of the other nonresonating poles can be neglected.

The influence of the nearest nonresonating pole can be estimated. There

$$x_{m-1} = [\omega_\mu - (m-1)\Omega]\tau_\mu = x_m + \Omega\tau_\mu \,. \tag{2.10}$$

The contribution of the pole of the order $(m-1)$ to the sum in Eq. (2.5) is approximately given by the term

$$-A_{\text{eff},j}((m-1)\Omega)\frac{\sin\psi_{m-1,j}}{(\Omega\tau_\mu)^2}\, x_m$$

if the other effectively field-independent contributions are absorbed into the constant background and $A_{\text{eff},j}(m\Omega)$. In order to estimate the size of the field shift arising from the neglect of the resonance of order $(m-1)$, we assume that $\Psi_{m-1,j} = \pi/2$ and $\psi_{m,j} = 0$, which yields the largest fractional shift. In that case the stroboscopic signal reaches its maximum at a value of x_m differing from zero by

$$\delta x = -\frac{A_{\text{eff},j}((m-1)\Omega)}{2A_{\text{eff},j}(m\Omega)} \frac{1}{(\Omega\tau_\mu)^2} \,,$$

from which a fractional shift of

$$\frac{\delta\omega_\mu}{\omega_\mu} = -\frac{A_{\text{eff},j}((m-1)\Omega)}{2A_{\text{eff},j}(m\Omega)} \frac{1}{(\Omega\tau_\mu)^3} \frac{1}{m} \tag{2.11}$$

is calculated. Under the effective conditions of our experiment the shift is expected to be

$$\frac{\delta\omega_\mu}{\omega_\mu} = -10^{-9} \,. \tag{2.12}$$

The cumulative influence of all other resonances is well below the 10^{-8} level.

E. Minimization of statistical error

The fractional statistical error in the determination of μ_μ/μ_p is given by

$$\frac{\Delta\omega_\mu}{\omega_\mu} = \frac{\text{constant}}{\sqrt{N}\, A_{\text{eff}}\omega_\mu\tau_\mu} \,. \tag{2.13}$$

The constant has been evaluated from the error matrix, assuming that the magnetic field was swept continuously over six line widths of the stroboscopic signal and neglecting correlation between the different fit parameters. Its value has been determined to be 3.

Near to a resonance, $\omega_\mu \approx m\Omega$, so clearly a high-order harmonic is preferable. But for a large value of m the effective asymmetry decreases, and there exists an optimum value for m at which the product $mA_{\text{eff},j}(m\Omega)$ reaches its maximum. Therefore, A_{eff} has to be calculated for the existing beam bursts and a suitable length of the stroboscopic gates has to be chosen.

The experimental beam burst can adequately be described by Eq. (2.6) with $\kappa = 0.13$. The re-

TABLE I. Intrinsic accuracy factor of the stroboscopic measurement as a function of the harmonic of the beam-burst repetition frequency, and corresponding quantity reduced by the finite time gate length—see Eqs. (2.13) and (2.7). $\kappa = 0.13$, $\lambda_j = 0.1$.

m	$me^{-(m\pi\kappa)^2}$	$me^{-(m\pi\kappa)^2}\sin(m\pi\lambda_j)/m\pi\lambda_j$
1	0.85	0.83
2	1.03	0.96
3	0.67	0.57
4	0.28	0.21

sulting values for $me^{-(m\pi\kappa)^2}$, proportional to $mA_{eff}(m\Omega)$, are listed in Table I as a function of m. Obviously, $m = 2$ is the best choice. In addition, one has to consider the influence of the finite gate length λ_j on the effective asymmetry, i.e., a reduction by $\sin(m\pi\lambda_j)/m\pi\lambda_j$. For that case $(m/A)A_{eff,j}(m\Omega)$—see Eq. (2.7)—is also listed as a function of m in Table I, third column. The optimum still corresponds to $m = 2$, and the reduction in accuracy is well tolerable.

The experimentally observed effective asymmetry was $A_{eff} = 0.16$. Together with a muon-decay asymmetry $A = 0.24$ as observed in a time-differential muon-spin-rotation (μSR) measurement using the same setup, the asymmetry reduction factor is $\frac{2}{3}$, while we had expected a factor of 0.51 from the measurement of the beam-burst structure. This discrepancy is not fully understood, but it can be explained by a nonuniformly distributed polarization inside the muon bursts.

By choosing $m = 2$ and neglecting nonresonating poles, the stroboscopic line shape is given by

$$N_j = N_0\lambda_j\left[1 + A_{eff}\,\frac{\sin(2\pi\lambda_j)}{2\pi\lambda_j}\,\frac{\cos\psi_j - x\sin\psi_j}{1+x^2}\right], \tag{2.14}$$

with $x = (\omega_\mu - 2\Omega)\tau_\mu$ and $\omega_\mu = (\omega_\mu/\omega_p)\omega_p$.

Equation (2.14) contains four unknown parameters, λ_j, A_{eff}, ψ_j, and (ω_μ/ω_p). Values for these parameters will be determined by fitting the experimental data with this formula.

III. EXPERIMENTAL SETUP AND DATA-TAKING PROCEDURE

A. Principal components of the setup

The general layout of the experiment is shown by Figs. 2 and 3. The principal components are the beam line (Sec. III B), the magnet (Sec. III C), and the target with the collimator and scintillation detector arrangement around it (Sec. III D). The target was of spherical shape (i.e., a spherical quartz ampoule containing liquid bromine) in order to get rid of small induced magnetic fields arising from a nonzero magnetic bulk susceptibility χ of the material (see Sec. II C). The particle detection assembly, its logic and associated electronics are discussed in Secs. III E and III F.

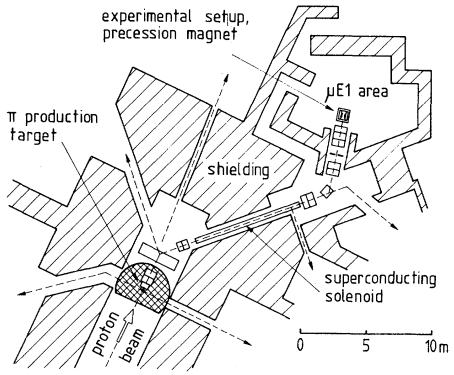

FIG. 2. Schematic layout of the pion/muon beam line used in the experiment ($\mu E1$ area). Broken lines indicate other secondary beams derived from the thick pion production target.

B. Pion/muon beam

The experiment has been carried out at the main superconducting muon channel of SIN. The pion/muon beam line is shown in Fig. 2. Charged pions leaving the thick production target (12 cm of beryllium) in the forward direction are collected by a magnetic quadrupole triplet and deflected according to their charge by a dipole magnet. The positive pions, deviated to the right, are focused by a quadrupole pair and injected into the superconducting solenoid (field strength 5 T, length 8 m, inner diameter 12 cm). In the solenoid the pions describe a stretched helix, and most of them decay. For the high π^+ momentum chosen (220 MeV/c), muons are emitted into a narrow forward cone of 11°. To obtain polarized muons (with respect to the beam axis) only muons from backward decay were accepted ($p_{\mu^+} = 125$ MeV/c). We used the $\mu E1$ beam line, composed of a dipole magnet mounted between two quadrupole doublets, an intermediate focus slit, and a quadrupole triplet which focuses muons on the stopping target.

In order to reduce muon stops outside of the bromine target, the beam was collimated down to 18 mm diameter (see Fig. 3). A degrader mounted inside the collimator (typically some 5 mm Cu followed by 5 mm Ta) was used to optimize the μ^+ stopping rate in the target.

The beam line configuration provided a high μ^+ flux through the collimator (2×10^6)/sec for a typical primary proton intensity of 40 μA), a polari-

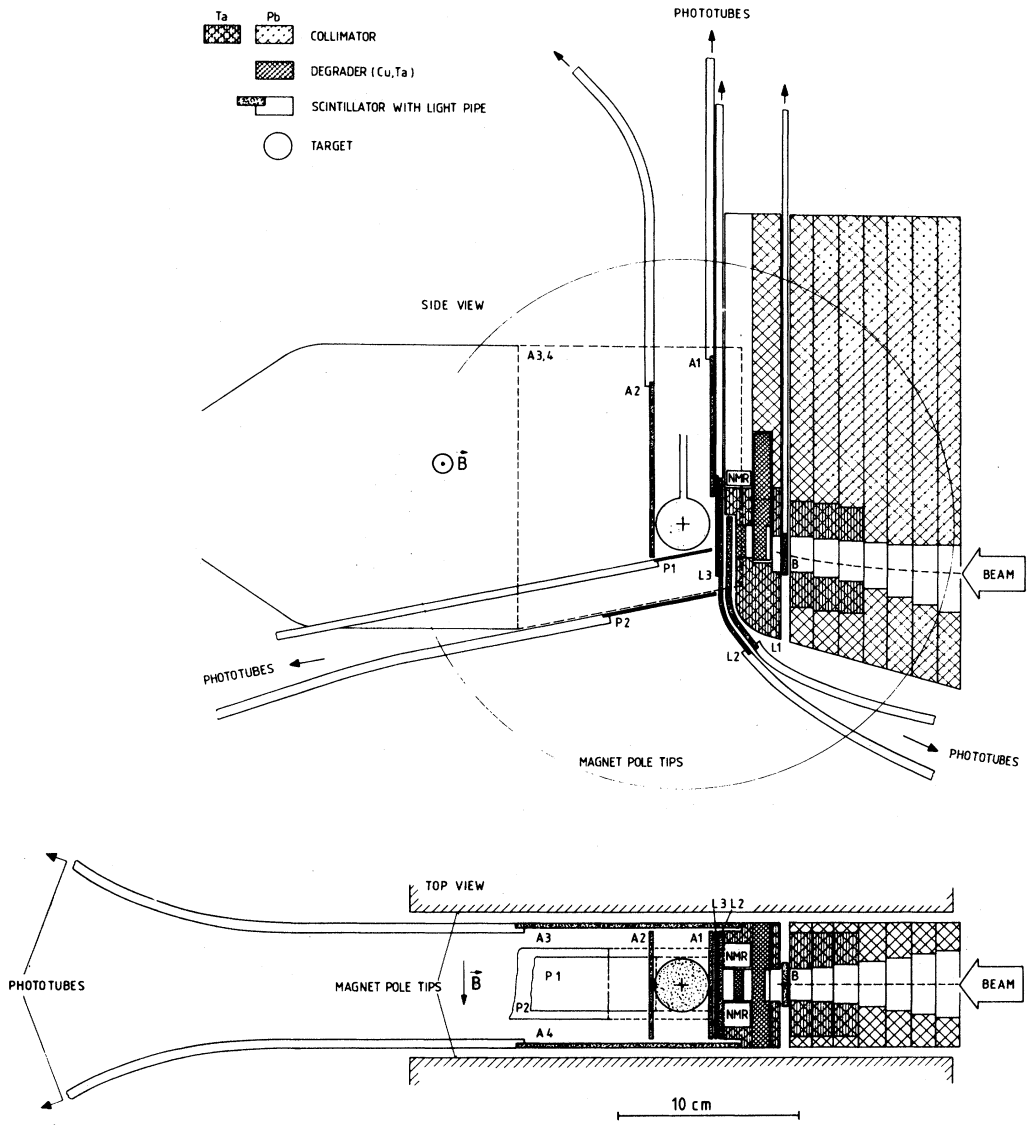

FIG. 3. Side and top view of the experimental arrangement (cuts). The diameter of the magnet pole faces is 30 cm. NMR indicates the location of stabilization and monitor NMR probes. Detectors P_1,P_2 constitute the positron telescope. Detectors L_1–L_3 and A_1–A_4 serve to veto muons and unwanted positrons, and B is the beam counter.

zation of 70%, and a negligible nonmuonic contamination. The beam-burst width, about 0.2 nsec. for protons at the production target, and essentially unchanged for the π^+ beam, increases, of course, for the muon beam, because of the π/μ velocity difference and the spread in the π decay location. The high momentum was chosen in order to keep the beam-burst width at an acceptable level: the width of the observed muon bursts was 4–5 nsec full width at half maximum (see Fig. 1).

C. Magnetic field

A 12-in. iron magnet (Varian type V4012-3B) with a pole gap of 83 mm provided a horizontal magnetid field of about 0.747 T necessary to obtain a muon-spin-precession frequency of about 100 MHz. The magnet was mounted on a hydraulic platform which allowed the adjustment of its height by remote control. A stabilized power supply (Varian type V2100B) provided the magnet current with an intrinsic stability of 10^{-5}. Two proton spin resonance systems were built: one system with fixed probe was used to stabilize the magnetic field; the second system with the probe mounted on a motor driven carriage served to scan and, in particular, to measure the field at the target center position. A third NMR probe was mounted near to the target. It was used during data taking

to monitor the regulation system. The electronics of the second system was alternatively connected by remote control to this monitor probe or to the scanning probe.

The initial spatial homogeneity of the magnetic field over the target volume (14 cm^3) was about 10 ppm; by use of a ten-current shim system, it was improved to ± 0.3 ppm.

1. The NMR systems

The two NMR systems are schematically shown in Fig. 4. They were similar in circuitry and layout to the calibration system used by the CERN Muon Storage Ring Collaboration.[11] The probe heads of the stabilizing and measuring NMR systems consisted of 5-mm-long polyethylene cylinders of 1.5 mm diameter, shrunken by heat around the rf coil. The probe heads contained a 0.035 molar solution of $NiSO_4$ in H_2O. Cylinder and field modulation coil were mounted inside a plexiglass frame and shielded by a Cu box.

The electronic circuitry is fully described in Ref. 11. It consists of the primary resonant *LC* circuit which is damped by energy absorption from the probe if proton spin resonance frequency and the externally applied radio frequency coincide. The resonance frequency of the *LC* circuit is automatically tuned to the external radio frequency so that asymmetric NMR resonances are avoided. The small amplitude modulation of the external magnetic field results in a differentiation of the absorption curve detected by lock-in technique. The output voltage of the lock-in amplifier as a function of the external radio frequency shows a dispersive shape. Its zero crossing determines the magnetic field in units of the proton spin resonance frequency. The fractional linewidth of ± 0.7 ppm (± 20 Hz at 31810 kHz) allows a determination of the line center with a reproducibility of ± 0.05 ppm. For the NMR regulation system the line was broadened by a higher concentration of paramagnetic ions. For this system a power amplifier supplied a current proportional to the lock-in output voltage to additional coils wound on the magnet pole pieces. Thus the magnetic field at the position of the probe head was stabilized. Tests using the measuring NMR system proved that the long-term stability of the magnetic field at the stabilizing probe head was 2×10^{-8}.

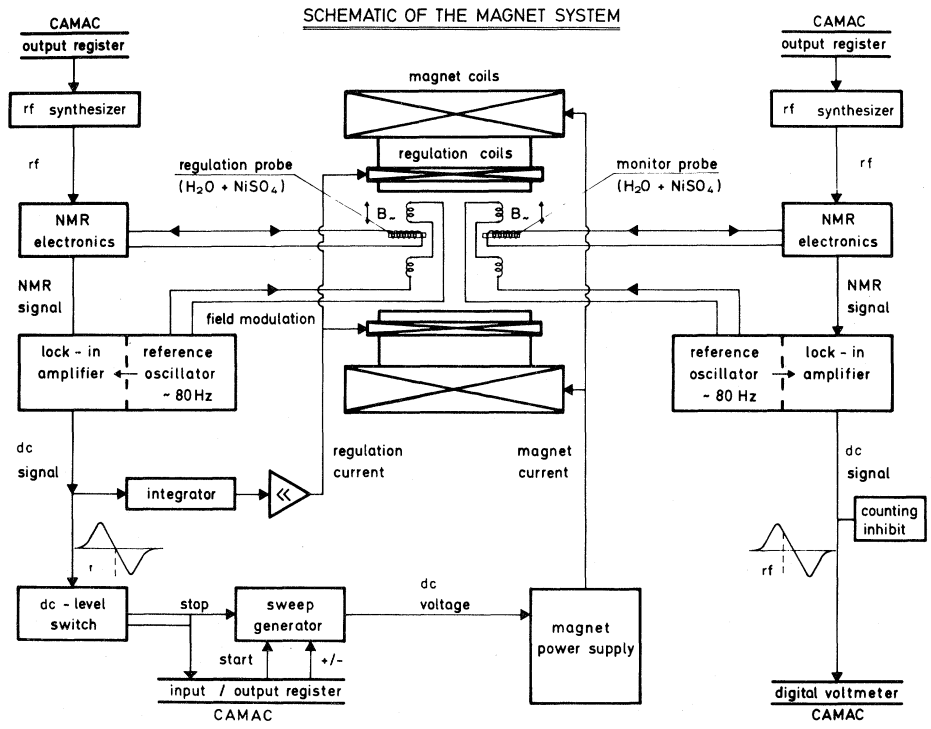

FIG. 4. Diagram of the NMR field control setup. One NMR system serves to stabilize the field at a given radio frequency ν_0 (corresponding to the zero crossing for the derivative of the NMR signal), the other monitors the field at a frequency $\nu_0+\Delta\nu$, chosen so as to produce a sizable amplitude for the derivative of the NMR signal, which is measured by an analog-to-digital converter. The dc signal from the first lock-in amplifier, besides producing the regulation current, is also used to stop the sweep generator, which shifts the main field to the next set point.

By the use of pick-up coils it was shown that short-term variations of the magnetic field, e.g., at 50 Hz or its harmonics, were also at this level or below.

2. *Field map*

Temperature variations of the magnet generated changes of the magnetic-flux distribution, e.g., a 2 °C temperature drop of the magnet cooling water increased the field at the target center by about 2 ppm (the distance from probe head to target center was 50 mm). Therefore the temperature of the magnet cooling water was stabilized by means of a controlled heat exchange with a secondary cooling circuit. In addition, the magnet was operated in a thermostatized hut. Temperatures of magnet cooling water, magnet yoke, and ambient air were continuously monitored by the data-acquisition system.

Maps of the magnetic field were obtained by the following procedure: The NMR measuring probe was driven to the target center, a complete NMR resonance curve was measured, and the central frequency was determined. For this frequency the analog output voltage of the lock-in amplifier was—for small deviations of the magnetic field—proportional to the deviation of the magnetic field from its value at the target center. The magnetic field distribution over the target volume was scanned by recording the lock-in error voltage at fixed lattice points. Their separation was 5 mm, corresponding to totally 113 lattice points over the target volume of 14 cm^3.

A current shim system was implemented which allowed a considerable improvement of the field homogeneity. Figure 5 shows its layout. Circular shims were chosen since they are best adapted to the symmetry of the magnet. For optimization of the shim currents, the NMR probe was steered along the coordinate axes and their diagonals. Probe position and lock-in error voltage were written by a two-coordinate recorder. Linear and quadratic parts of the inhomogeneity were estimated and compensated by the corresponding shim current. After iterative tuning, a field homogeneity of about ±0.3 ppm over the target volume was achieved. In the course of the experiment the magnetic field at the target center was checked regularly; the field stability for individual runs was estimated from the observed residual drifts of the magnetic field (typically 3×10^{-8}).

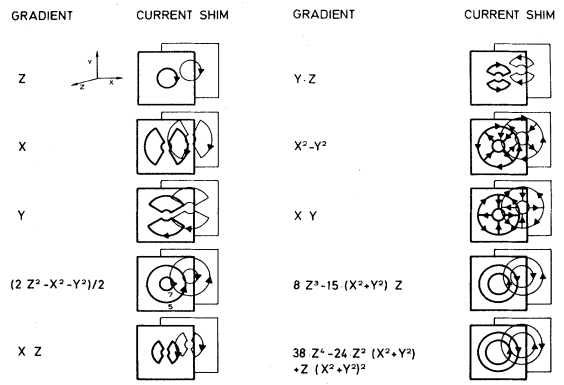

FIG. 5. Ten-current shim system used to improve the magnetic-field homogeneity. The field gradients which can be independently corrected are indicated (Z corresponds to the magnet axis). The achieved field homogeneity over the target volume was ±0.3 ppm.

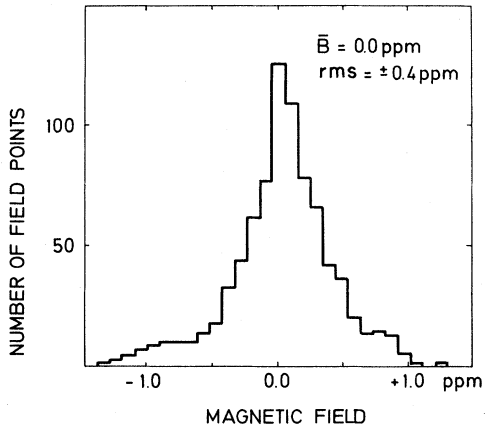

FIG. 6. Histogram of the magnetic-field distribution over the target volume. It corresponds to the superposition of eight field maps (corrected for drifts at the target center) taken in the course of six days. The rms deviation of the mean value amounts to ±0.4 ppm.

The magnetic-field distribution over the target volume was measured daily. On a few occasions the rms deviation of the field from its mean had deteriorated to about 0.5 ppm. The shim currents were then reoptimized and a new field map was taken.

Figure 6 shows a summed histogram of eight magnetic-field distributions over the target volume taken in the course of six days. The individual histograms were corrected for residual drifts of the magnetic field at the target center. The rms deviation of the magnetic field from its mean value averaged over a target volume of 14 cm^3 and over six days was ±0.4 ppm. Various hypothetical muon-stop distributions, even if highly improbable, led to mean values of the magnetic field which differed at most by 0.08 ppm from the linear average of all field values. Therefore an error of 0.08 ppm was assigned to the magnetic field on account of our ignorance on the muon stop distribution.

3. *Absolute calibration*

For the absolute calibration[12] of the measuring probe used to determine the magnetic field, a series of unshielded calibration probes made out of different materials (teflon, polyvinyl chloride, glass), of different lengths (20–80 mm), and of different diameters (1–3 mm) were built. The cylindrical probes had a length to diameter ratio of more than 15 : 1. Hence they can be regarded as infinitely long. The probes were mounted inside an open pair of Helmholtz coils which modulated the external magnetic field by a few mG at a frequency of 10–20 Hz. The rf coils (six turns) covered an active length of 4 mm. The results obtained by the different calibration probes agreed within 0.12 ppm (rms deviation). The center frequency obtained from the measuring probe was found to be 0.80 ppm lower than the average value derived from the calibration probes.

As mentioned earlier, measuring and calibration probes were filled with distilled water, but paramagnetic ions (0.03 mol $NiSO_4$) were added to reduce the relaxation time. The frequency shift due to the presence of the paramagnetic ions was determined in a conventional high-resolution NMR spectrometer and was found to be 0.35 ppm. Finally, the proton resonance frequency had to be corrected for the diamagnetic shielding of the magnetic field and the probe shape dependent demagnetization of the probe, which is a consequence of the nonzero bulk magnetic susceptibility. The diamagnetic shielding was determined by Phillips, Cooke, and Kleppner to a value of 25.790(14) at 37.4 °C.[13] Using Hindman's values for the temperature dependence,[14] we obtain at 25 °C σ_{H_2O} = 25.64(3) ppm.

For a long circular cylinder transverse to the magnetic field, the bulk-susceptibility correction amounts to −1.51 ppm.

The retained corrections, the resulting value σ_{NMR}, and their errors are listed in Table II. The errors are added in quadrature because of the statistical nature of their occurence.

The corrections do not contain the difference between the magnetic fields at target center and at the position of the regulation probe. This difference and its error are accounted for in the evaluation of ω_μ/ω_p from the data.

TABLE II. Corrections to NMR frequency of the field-measuring probe.

Diamagnetic shielding σ_{H_2O}	+25.64(3) ppm
Bulk susceptibility	− 1.51(4) ppm
Paramagnetic ions	+ 0.35(5) ppm
Calibration	+ 0.80(12) ppm
Field map	0.00(8) ppm
Total correction σ_{NMR}	+ 25.28(16) ppm

D. Target arrangement

The utilizable magnetic-field volume essentially determined target and beam dimensions. The target arrangement is shown in Fig. 3. The liquid bromine was contained in a spherical quartz ampoule of 30 mm diameter and 0.2 mm wall thickness. Quartz was chosen because the free precession amplitude of muons stopped in it is known to be small.[15] The target was mounted at the center of the pole gap of the magnet.

The beam collimator was built out of four Pb and three Ta plates, each 15 mm thick, which could be independently positioned between the pole pieces to optimize the beam passage, allowing for the slight curvature of the beam in the field region. A further Ta block, closest to the target and about 25 mm thick, contained a Cu degrader in the form of a revolving wheel with six sections of different thickness (0–8 mm Cu). In addition, 5 mm of Ta was always placed in the last hole of the collimator behind the Cu wheel. The reason for the use of Ta is given in Sec. IV B. A scintillation detector B, placed between the last Ta plate and the degrader block, served as beam counter. The degrader block also housed the two fixed NMR probes.

Close behind degrader and collimator, the set of detectors L_1, L_2, L_3, and A_1 was mounted. The detectors registered particles that originated from the degrader/collimator region. Their geometrical shapes and positions were optimized for best detection efficiency. All scintillators were made out of NE102. Their thickness was 3 mm, except for L_1 and P_1, which were only 1 mm thick to reduce the fraction of particles stopping in them.

The distance between target and collimator was made as small as possible. Approximately 40% of the muons passing the collimator were stopped in the bromine target. The two lateral detectors A_3 and A_4 covered the major part of the pole caps, and the detector A_2 registered particles coming from (or going) behind the target. The positions of the degrader wheel, the target ampoule, the detector A_2 and of the NMR measuring probe were set by remote control.

E. Detection and identification of decay positrons

The plastic scintillation detectors and the electronic circuitry served to count the number of incoming muons and their stop rate, to identify positrons from the decay of muons stopped in the target, to discriminate these positrons against those

which originated from muons stopped elsewhere, and to determine the timing of accepted positrons. A positron telescope $P_1 \cdot P_2$ detected decay particles originating from the target in a solid-angle fraction of the order of 4%. A box formed around the target by the L and A counters eliminated by anticoincidences particles registered by the positron telescope which did not come from the target. The accepted events were basically defined by the logical operation

$$P_1 \cdot P_2 \cdot \overline{(L_1+L_2+L_3+A_1+A_2+A_3+A_4)} .$$

The rate was 27 000/s for a typical proton beam intensity of 40 μA.

A schematic diagram of the detectors and the positron identification electronics is shown in Fig. 7. The components essential for the measurement are drawn with solid lines.

XP2020 photomultiplier tubes were used on standard SIN bases, optionally supplied with an additional −1 kV dynode voltage for better stability at high rates. The anode signals went through fast amplifiers (LeCroy 612) before entering the different discriminators. For the logical section of the electronics LeCroy 621S discriminators were mostly used. The pulses from counters L_1–L_3 and P_1–P_2 were fed into two separate discriminators of high (H) or low (L) thresholds, respectively. The high-threshold discriminators accepted pulses from low-momentum muons, but rejected pulses originating from minimum-ionizing positrons. For the veto signals (L, A, and P_H events), the burst-guard (bg) feature of the discriminator was used.

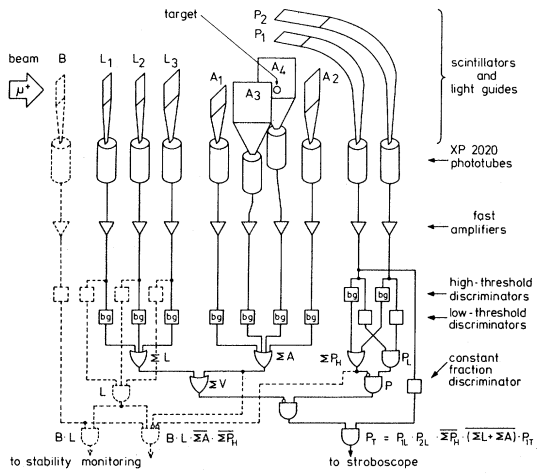

FIG. 7. Schematic diagram of the particle detection electronics. The essential part (solid lines) selects and prepares the accepted positron signals for the stroboscope. Additional components (dashed lines) are used for stability checks.

The coincidence $P_L = P_{1L} \cdot P_{2L}$ was vetoed by (muon) events $P_H = P_{1H} + P_{2H}$ to define positron events P. The sum of L events plus the sum of A events gave "veto" events $\sum V$. The coincidence $P \cdot \overline{\sum V}$ thus defined logically accepted decay positrons. To get the best possible time resolution for the stroboscope (see III F), $P \cdot \overline{\sum V}$ was used to gate a timing signal P_{1T}, generated from a constant fraction discriminator (Ortec 473A) fed from the positron detector P_1. The timing signal of accepted positrons P_T was so logically defined by $P \cdot \overline{\sum V}$, but synchronized on P_{1T}. This signal was then processed further by the stroboscope.

For setup, tuning, and stability checks, additional components were also used. The most important of them are sketched by dashed lines in Fig. 7. They gave the beam signal $B \cdot L = B \cdot L_{1H} \cdot L_{2H} \cdot L_{3H}$, and the stopped-muon signal

$$B \cdot L \cdot \overline{\sum A} \cdot \overline{\sum P_H} .$$

In addition to P_T, used also as normalization, 20 signals (coincidences, sums, single-detector rates, etc.) were directly fed into CAMAC scalers and recorded during the measurement for stability checks.

F. Stroboscope

The timing signals of accepted positron events were binned according to their timing with respect to the phase of the master frequency, i.e., of the quartz oscillator frequency driving the rf accelerator cavities. The electronic circuitry binning the positron events consisted of ten contiguous nonoverlapping gates $G_i(t)$ of lengths λ_i and phases ϕ_i satisfying the relations

$$\sum_{i=1}^{10} G_i(t) = 1, \quad G_i(t) \cap G_j(t) = 0 \quad \text{for } i \neq j ,$$

or (3.1)

$$\sum_{i=1}^{10} \lambda_i = 2\pi/\Omega .$$

Clearly, the ten gate lengths and phases of the "stroboscope" are related. Under ideal circumstances they can be described by totally ten parameters instead of twenty, e.g., by nine gate lengths and the phase of the first gate relative to the phase of the master frequency.

The electronic circuitry of the stroboscope is depicted in Fig. 8. Each positron event was split into two subsequent pulses A and B of 10 nsec separation. The pulses fell into two series of five partly overlapping data gates derived from the master frequency. Routing coincidences identified the positron A and B pulses. From the two series of five data gates ten contiguous nonover-

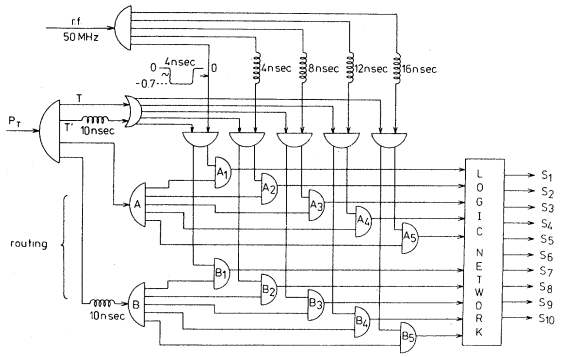

FIG. 8. Schematic circuitry of the stroboscope. Two sets of five gates delayed by 10 nsec relative to each other, each set covering roughly the 20 nsec period between two beam bursts, are derived from the 50 MHz master oscillator. The accepted positron signals P_T are brought into 10 coincidences with these gates. The outputs are combined in such a way by a logic network to produce 10 positron signal channels, corresponding to 10 nonoverlapping and gap-free time windows covering exactly the beam-burst repetition period.

lapping stroboscopic gates were constructed by sequential coincidences and anticoincidences. Bench tests showed that there was a one-to-one correspondence at the level of 10^{-5} between positron counts fed into the stroboscope and count rates in the ten stroboscopic gates. Two of these stroboscopes were set up in order to allow for systematic checks which will be discussed later on. The outputs of the stroboscopic gates were fed into CAMAC scalers and recorded by a PDP-11/40 processor.

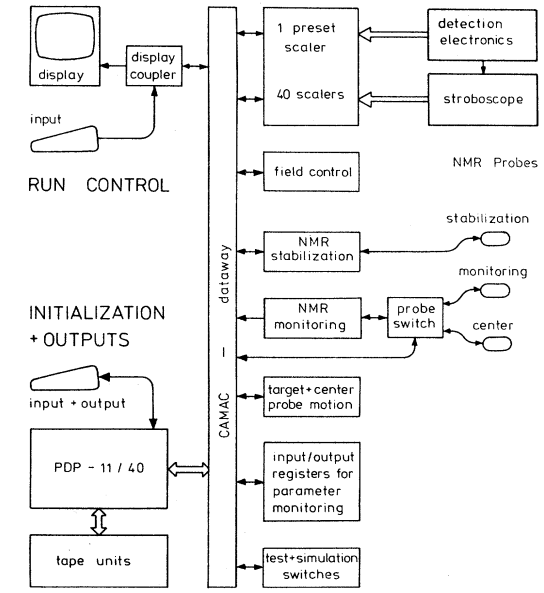

FIG. 9. Control and data-acquisition system for stroboscopic measurement. A DEC PDP-11/40 computer controls the experiment via a CAMAC system.

G. Measuring procedure

The automatic data-taking procedure was controlled by a DEC PDP-11/40 computer via CAMAC electronics. The data flow and control scheme is shown in Fig. 9.

In the initialization phase of the acquisition program, the magnetic field points to be scanned were selected and a preset value for the number of accepted positron counts per field point was entered. Parameters related to stability checks of field, rates, beam-burst phase, etc., had also to be given.

At the measurement start command, a slow field sweep was initialized (a CAMAC output register controlled a ramp generator driving the magnet power supply) to bring the field towards its required value. At the same time the frequency generators of the two NMR circuits were set at the corresponding expected values (taking into account the shift due to the small field difference between the two probe locations). As soon as the field reached the working domain of the NMR regulation, this circuit sent an interrupt to the processor to stop the field sweep and, if necessary, to correct for an overshoot. The NMR monitor circuit tracked the field. After a preset delay, counting was enabled if the field was correctly stabilized.

During a data-acquisition period, events from the 20 gates of the two stroboscopes, from 20 control channels (including a measurement of the elapsed time), and the total number of accepted positron events were counted. When this last number had reached the fixed preset value, counting was stopped. This assured an automatic normalization of all counts for different field values. Such an acquisition period took typically 45 sec. The processor transfered the 41 scaler contents into the memory and the scalers were reset. To each field point (up to 40, but typically 29) corresponded a set of memory allocations. Additional parameters (monitor or central field registered by the monitor circuit, burst phase, etc.) were similarly stored. Thereupon, a field change to the next field point was initialized. On the average, some 15 sec elapsed till new counting started.

Before starting data acquisition at a new field value, parameters like beam-burst phase, magnet temperature, etc. were tested and the procedure was interrrupted if the stability requirements were not met. At any time a hardware inhibit could interrupt counting if the magnetic field was not properly regulated and/or if the μ^+ beam

dropped below a preset intensity.

When acquisition at the last field value was completed (cycle end), the data accumulated in the memory were written on tape. Subsequently, the cycle was repeated with a reversed scan direction.

A measurement of the central field, implying a change of target and NMR probe positions, could be either initialized on request or automatic for scheduled field points.

The frequency of the master oscillator driving the rf cavities of the accelerator was measured by a digital frequency counter (Hewlett-Packard 5327B). The reference frequency for this counter was supplied by the rf synthesizer used to determine the proton NMR frequencies. The master oscillator proved to be stable to $\pm 10^{-8}$. Possible slight absolute inaccuracies of the reference rf synthesizer cancel completely in the determination of frequency ratios.

H. Data

Data were taken using three different types of targets:

(i) Liquid bromine where P_2O_5 and HBr was added in order to remove a water contamination, (ii) liquid bromine which was contaminated by a small amount of water, and (iii) a distilled water target. The chemical processes which muons undergo in these targets are different, they are discussed in Sec. V. The data-taking period extended over 63 h for target (i), 71 h for target (ii), and 45 h for target (iii), which includes the time necessary for field scans and field measurements at the target center.

In addition, target-empty runs were taken in order to determine the stroboscopic background (14 h).

Figure 10 shows the stroboscopic signal in two of the ten stroboscopic gates. The data presented in this figure were collected in 61 scanning cycles corresponding to about two days of running time. The solid line represents a fit to the data, the fitting routine being described in the following section.

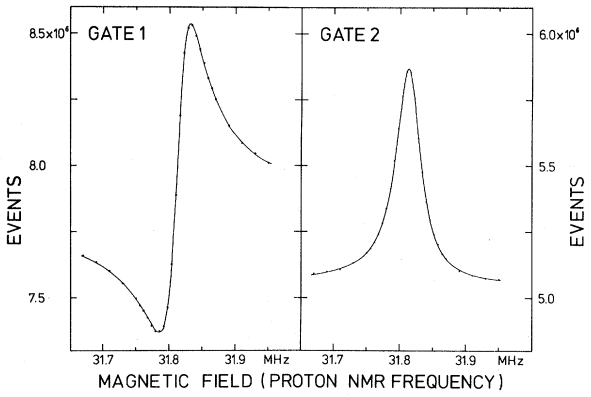

FIG. 10. Stroboscopic signal from two out of the ten stroboscopic gates. The abscissa is the externally applied magnetic field, in proton NMR frequency units. The dots are the measured number of events for the 29 field values. The dot radii correspond to the statistical errors. The solid lines represent a fit to the data, determining the uncorrected ω_μ/ω_p parameter to a precision of ± 0.7 ppm. The data shown were collected in about two days of running time.

IV. DATA ANALYSIS

A. Objectives

The data analysis has to yield the value (and its error) of the magnetic field (i.e., ω_p) at which the muon spin precesses at the second harmonic of the beam-burst repetition frequency (i.e., ω_μ). Here we discuss a number of analysis routines and the results obtained when applied to the experimental data.

The analysis routines make use of the function-minimization program MINUIT.[16] The fitting procedure is based on a minimization of the χ^2 function

$$\chi^2 = \sum_i \frac{[N_{\text{exp}}(i) - N_{\text{theor}}(i)]^2}{\sigma^2(i)}, \tag{4.1}$$

where $N_{\text{exp}}(i)$ are the counts in the ith channel and $N_{\text{theor}}(i)$ is given by a line-shape theory. $\sigma(i)$ represents the expected variance. For high and statistically distributed count rates of independent events, $\sigma^2(i) = N_{\text{theor}}(i)$.

B. The influence of experimental imperfections on the line shape

The basic features of the line-shape theory were developed in Sec. II, but additional effects caused by practical imperfections of the experimental set-up have to be incorporated. Here we discuss the influence of the finite veto pulse lengths and of phase instabilities of the stroboscope or the muon beam. The effects of background positrons originating from muons which were not stopped in the target, and of the change in the positron trajectories resulting from the magnetic field sweep are also treated.

1. Detection-efficiency modulation

Particles detected in the positron telescope are vetoed if a coincident particle passes through any scintillation counter surrounding the target. Since the muon beam has a burst structure, there is a periodic chance that otherwise accepted positrons

will be rejected because of random coincidences with uncorrelated incoming muons. The detection efficiency of the stroboscopic gates therefore depends on their phase relative to the muon beam bursts, and the gate lengths of those stroboscopic gates which are active when the muon beam bursts arrive at the target seem to be smaller than measured in bench tests. The mean phases of the corresponding gates do not, however, change and therefore the fixed relation between phases and gate lengths is distorted. The modulation of detection efficiency was directly measured by vetoing statistically distributed events from a radioactive source with muons entering the target. The size of the effect (several 10^{-3}) was compatible with the size of the efficiency modulation which was found by fitting the experimental data.

2. *Prompt vetoes*

The veto pulses derived from incoming muons veto also those positrons which were emitted within some 10 nsec after the stop of the correlated muon. Therefore only muons living longer than the pulse duration of prompt vetoes contribute to the stroboscopic signal. A time delay of 10 nsec corresponds to a 2π rotation of the muon spin at the resonance frequency. But at the lowest or highest magnetic field points scanned during data taking, the polarization vector has acquired a phase shift of ∓ 1.6 degrees. The inclusion of this effect in the line-shape theory implies that in Eq. (2.14) the phase ψ_j is now slightly dependent on the magnetic field. This effect was optionally accounted for in the fitting routines by a straightforward modification of the theory, with the time delay t_D as free parameter. However, the χ^2 minimization preferred to adjust t_D to zero and to increase the muon lifetime by about 10^{-3}, unless τ_μ was kept at its physical value.

3. *Curvature of positron tracks*

The trajectories of positrons emitted in the decay of stopped muons are curved due to the magnetic field. This has two effects.

First, there is a field-dependent low-energy threshold for positron detection. Since the number of accepted positrons is normalized, this results in a larger fraction of energetic positrons and hence a higher asymmetry at the high-field side of the resonance. Evidence for this effect was derived from the slightly field-dependent number of stopped muons necessary to obtain the preset positron counts. Assuming a linear dependence of the change in asymmetry across the resonance, it can be shown that the resonance position in one particular stroboscopic gate should be shifted by

$$\frac{\delta\omega_\mu}{\omega_\mu} \approx \frac{1}{7\omega_\mu\tau_\mu}\frac{\delta A_{\text{eff}}}{A_{\text{eff}}}\cos 2\psi_j .$$

A calculation indicated that this effect should not be detectable, and, indeed, it was not found when it was allowed for in an analysis routine. In any case, the effect vanishes when data from all ten gates are considered.

Second, the mean positron detection angle is phase shifted depending on the magnetic field and the positron energy. For a positron energy of 30 MeV the phase shift differs by ∓ 0.3 degrees when going from the lowest- to the highest-field points. This effect is therefore smaller than the field-dependent phase shift discussed in Sec. IV B 2.

4. *Phase instabilities*

(*a*) *The stroboscopic gates.* The stroboscope consists of ten contiguous gates of about 2 nsec widths. Clearly, high leading-edge stability of the coincidences is required to guarantee optimum performance. The leading-edge stability of one of the two stroboscopes was evidently worse than that of the other one, resulting in a larger variance of the corresponding stroboscopic data. Bench tests showed also that this stroboscope introduced a systematically larger phase jitter. Therefore data derived from this stroboscope were not used in the final analysis.

(*b*) *The muon beam.* Phase instabilities of the muon beam itself may also lead to considerable distortions of the stroboscopic signal. Therefore one stroboscope was phase locked to the pick-up signals induced by the primary proton beam. The purpose was to investigate if possible effects of proton-beam phase variations leading to a phase jitter of the muon beam bursts can be reduced or avoided. In the course of the experiment it became clear that under stable beam conditions there was no difference between data from the stroboscope phase locked to beam bursts or from the stroboscope locked to the quartz oscillator. If, however, the proton beam was unstable, either due to changes of the beam phase in setup periods, or because of plasma oscillations in the proton source, the stroboscopic signal was grossly distorted, resulting in a largely increased variance. Therefore the phase of the beam bursts relative to the phase of the master oscillator was monitored continuously in the course of the experiment, and only those data were evaluated where the beam jitter was tolerable. Small residual phase jitters were averaged out by scanning through the resonance several times. This residual phase jitter led to a slightly increased statistical variation of count rates, and a ratio of χ^2/degrees of freedom greater than one has to be expected.

5. *Stroboscopic background*

Positrons originating from muons which were not stopped in the liquid-bromine target contribute to the stroboscopic signal, but the phase of the signal as well as the resonance field value will be different. A low background contribution was therefore a major concern throughout the experiment. Target, detector, and beam geometry in the pole gap, as well as the detection electronics were carefully optimized for that purpose.

An estimate for the background contribution was obtained from the positron rate with target removed: it corresponded to about $\frac{1}{45}$ of the accepted rate. This target-out rate was attributed to decay positrons from muons stopped in the wrappings of the scintillation counters or in one of the positron counters, or to residual inefficiencies of veto counters against positrons from muons which had stopped, e.g., in the collimator hole, a region of very high muon stopping density. Yet muons stopped in the above-mentioned materials are partly depolarized and the asymmetry of that stroboscopic background signal A_B is reduced. The positron rate from muons stopping in the quartz ampoule amounted to about 8% of the full stop rate. Their contribution to the stroboscopic signal was negligible.

The effect of a stroboscopic background on the value of ω_μ/ω_p was investigated by computer simulation. To the stroboscopic signal of amplitude S with a position corresponding to the p NMR resonance frequency ω_S, an artificial stroboscopic background of amplitude B with a position corresponding to the NMR frequency ω_B and a phase shift ϕ between stroboscopic signal and background was added (ϕ representing the shift in the telescope detection angle for the "background positrons" compared to the "signal positrons", due to the different geometrical origines of signal and background). By fitting these data a "measured" resonance frequency ω_M was obtained (the fit gives ω_μ/ω_M, where ω_μ is constantly twice the beam-burst repetition frequency). ω_M was found to satisfy the relation

$$\frac{\delta\omega_p}{\omega_p} \equiv \frac{\omega_M - \omega_S}{\omega_S} = \frac{B}{S}\,\frac{\omega_B - \omega_S}{\omega_S}\cos\phi\,, \tag{4.2}$$

which was also derived analytically.

Obviously B/S should be made as small as possible and the position of the stroboscopic background signal should be as close as possible to that of the main signal. Since it was suspected that a sizable fraction of the background originated from undetected and therefore unvetoed positrons from the collimator hole region, we used tantalum for the relevant part of the collimator and for the fixed degrader section closest to the target (it is known that the Knight shift for protons in Ta—at least in the dilute-concentration limit—is compatible with zero[17]).

Target-empty runs were carried out in order to determine resonance frequency, effective asymmetry, and phase shift of the background signal. The ratio of positron count rates (target empty)/(target full) N_B/N_S was $\frac{1}{14}$. The following values were measured:

$$\begin{aligned} &\frac{\omega_S - \omega_B}{\omega_S} = -(20 \pm 25)\ \text{ppm}\,, \\ &\phi = -(0.4 \pm 0.4)\,, \\ &A_B/A_S = 0.15\,. \end{aligned} \tag{4.3}$$

Consequently,

$$\frac{B}{S} = \frac{N_B}{N_S}\,\frac{A_B}{A_S} = 0.15/14 = 0.0107\,. \tag{4.4}$$

Hence a final correction of

$$\sigma_{BG} = -\frac{\delta\omega_p}{\omega_p} = -(0.20 \pm 0.25)\,\text{ppm} \tag{4.5}$$

was applied to account for the stroboscopic background.

C. Analysis routines

A major advantage of the stroboscopic method is the strong correlation of results obtained in the different stroboscopic gates. This correlation allows valuable cross checks on the consistency of data sets, and it allows one to detect and to control systematic effects which otherwise may lead to systematic errors. This correlation can technically be exploited in different ways, therefore more than ten different analysis routines were written and used to evaluate ω_μ/ω_p from the data. Here we present the main ideas of some of these analysis codes and the results obtained by them.

Without making use of the correlation mentioned above the data may be fitted by a sequential fit to the ten stroboscopic gates. For each gate j four free parameters $(\omega_\mu/\omega_p, A_{eff}, \lambda, \psi)_j$ are required, so totally 40 parameters are used to fit the data. Hence this routine is designated as SF40 (sequential fit with 40 parameters). The results for ω_μ/ω_p from the ten individual gates had a χ^2 per degree of freedom (χ^2/N_F) of typically 1.0–2.0, but no dependence of ω_μ/ω_p on the phase ψ_j of the stroboscopic gates was detected. This showed that the changes of asymmetry and of positron trajectories across the resonance (discussed in sec IV B 2 and IV B 3) do not affect our result at the present level of precision. The increased variance was attributed to statistical

TABLE III. Results for ω_μ/ω_p obtained by use of different analysis programs. In most cases, we merely give the last three significant digits of ω_μ/ω_p and the error (in parentheses). Beneath this, we give χ^2/N_F and N_F: Target: Br_2 contaminated with H_2O. Corrections for muon and proton field shieldings and for stroboscopic background not yet applied.

Run	*SF*40	*GF*31	*GF*12	*GF*22	*GF*46
501	3.183 3308(46)	295(45)	314(61)	317(44)	292(63)
		1.02	2.09	1.04	0.98
		230	249	239	215
505	337(45)	340(46)	358(72)	346(45)	317(65)
		1.35	3.65	1.41	1.29
		230	249	239	215
506	322(43)	343(41)	301(72)		375(72)
		1.09	3.64	330(36)	1.23
		230	249	1.30	215
507	351(61)	350(61)	339(92)	239	306(105)
		1.21	3.00		1.30
		230	249		215
510	273(46)	293(40)	290(73)	289(44)	226(70)
		0.97	3.48	1.11	1.03
		230	249	239	215
511	442(51)	454(51)	442(68)	443(55)	413(73)
		0.99	1.96	1.04	0.99
		230	249	239	215
513	435(60)	413(62)	388(85)	393(64)	399(91)
		1.54	3.30	1.71	1.60
		230	249	239	215
Average	3.183 3344(19)	346(18)	346(28)	341(19)	327(28)
	1.53	1.44	0.58	1.18	0.82
	6	6	6	5	6

TABLE IV. Results for ω_μ/ω_p obtained by use of different analysis programs in the same format as Table III. Target: Br_2 with H_2O contamination removed. Corrections for muon and proton field shieldings and for stroboscopic background not yet applied.

Run	*SF*40	*GF*31	*GF*12	*GF*22	*GF*46
518	3.183 3200(70)	154(70)	149(89)	170(81)	190(67)
		1.21	2.17	1.18	1.12
		230	249	239	215
519	315(66)	293(65)	301(81)	272(67)	147(94)
		1.21	2.13	1.30	1.23
		230	249	239	215
520	226(55)	254(56)	227(94)	226(60)	221(78)
		1.25	4.16	1.41	1.32
		230	249	239	215
528	192(42)	221(49)	205(72)		248(94)
		1.68	4.84		1.14
		230	249		215
529	201(46)	249(48)	210(74)	207(23)	230(61)
		1.02	3.29	1.55	0.94
		230	249	239	215
531	194(40)	174(45)	208(75)		204(55)
		1.24	4.53		1.02
		230	249		215
Average	3.183 3211(20)	220(22)	217(33)	212(20)	208(29)
	0.60	0.73	0.34	0.39	0.17
	5	5	5	3	5

phase jitters of the beam bursts or stroboscopic gates. It was accounted for by increasing the statistical error in ω_μ/ω_p by $(\chi^2/N_F)^{1/2}$ whenever this value was larger than one. The variance of the average value was estimated from the variance of the individual results and from their distribution. The larger one of these two values was assumed to represent the "true" variance. The variance of the proton spin resonance frequencies at the target center obtained during a particular run was calculated, and then the final statistical error of the run evaluated.

Tables III and IV show the values of ω_μ/ω_p and their errors for all accepted data runs obtained by use of SF40 and other analysis routines.

A simultaneous fit to all data gates is called a global fit; 31 parameters are needed if ω_μ/ω_p is required to assume the same value in all ten gates and $(A_{eff},\lambda,\psi)_j$ are all allowed to vary freely in the fit. The results of this fit (GF31) are presented in Tables III and IV. The errors given are again scaled by the square roots of χ^2/N_F which are also listed.

The ten phases, gate lengths, and asymmetries are, however, not independent [Eqs. (2.5), (3.1), and (A16)]. The asymmetries in individual gates can be calculated from their lengths and the global asymmetry, and the ten gate lengths and ten phases are related. So the total number of free parameters reduces to twelve: ω_μ/ω_p, A_{eff}, nine gate lengths, and one global phase.

The results obtained by the analysis routine GF12 are listed in Tables III and IV. They show by their large values of χ^2/N_F that the underlying line-shape theory is not yet totally adequate. The rigid link between gate lengths, phases, and asymmetries is obviously weakened by effects which are not accounted for in this theory.

In Sec. IV B we discussed the influence of several experimental imperfections on the line shape. Here we will discuss their treatment in the data analysis. The modulation of the detection efficiency by random coincidences of positrons with incoming muons (IV B 1) was incorporated into the line-shape theory. The modulation of detection efficiency is periodic with the beam-burst repetition frequency. It can hence be described by a Fourier series. In this development we kept the first five Fourier components (corresponding to ten real variables), because at most ten variables can be determined from the efficiencies of ten stroboscopic gates. Thus the total number of free parameters was 22: ω_μ/ω_p, A_{eff}, nine gate lengths λ_j, one global phase, and five complex Fourier coefficients describing the modulation of detection efficiency. This analysis code was designated as GF22; its results are listed in Table III and IV.

We tried to take into account systematic phase shifts across the resonance as well as phase instabilities of stroboscopic gates and muon beam. At a given value of the magnetic field, data were taken for a period of about one minute, but the magnetic field was scanned through the resonance in typically half an hour. If the relative phase between stroboscope and beam bursts was stable over a minute, but slightly unstable over half an hour, then it is useful to fit the global phase of the stroboscope relative to the beam bursts not only for the complete run, but for the individual magnetic field values. Hence the number of free parameters increases by the number of magnetic field values minus one. The global phases at the individual magnetic-field points had, indeed, a large variance. Nevertheless, χ^2 was not dramatically reduced in these fits, indicating that short time phase jitters were also important. A systematic phase shift across the resonance was detected, but it was highly correlated with τ_μ. However, no correlation with ω_μ/ω_p was found. Therefore we conclude that the assumption of constant phases ψ_j does not affect our final result.

It should be mentioned that the stability of the MINUIT program in approaching the "true" minimum suffered when up to 55 parameters were allowed to vary. Although χ^2/N_F was consistently lower, the error assigned to ω_μ/ω_p increased by up to a factor of two. As an example, the results of GF46 are presented in Tables III and IV. This program optimizes the values of ω_μ/ω_p, A_{eff}, nine gate lengths λ_j, five complex Fourier coefficients for the detection efficiency modulation, 23 phases at the more central values of the magnetic field, and two phases at the remaining low- and high-magnetic-field values. χ^2/N_F is slightly reduced but the overall error assigned to ω_μ/ω_p is larger than those obtained by the other analysis codes. Therefore we do not feel that we were able to control analysis codes of this type sufficiently well.

We searched for systematic changes in the asymmetry by allowing phases and asymmetries to vary for all magnetic-field points. This analysis code had 80 parameters, more than could be handled by MINUIT. Therefore, ω_μ/ω_p, A_{eff}, and ten gate lengths and phases were fitted by MINUIT. Then 29 phase shifts and 29 asymmetry shifts for the individual magnetic field points were fitted by the χ^2-minimization programme VA04A. After a few iterations the procedure converged. The systematic change of phase across the resonance found by this analysis code was compatible with the results of GF46. A magnetic-field-dependent change in asymmetry was not detected.

Finally, we want to point out that in all global fits t_D and τ_μ were optional variables. For the results of Tables III and IV, they were fixed at their physical values.

The distribution of values for ω_μ/ω_p obtained by use of any of the different analysis programs is compatible with the statistical expectation based on the errors of the individual runs [which are scaled by $(\chi^2/N_F)^{1/2}$]. Hence weighted average and its error can be calculated, and the results obtained by using different analysis programs are presented in the last lines of Tables III and IV.

The comparison of these totally consistent results shows that the neglect of systematic effects in the line-shape theory does not affect dramatically the final result for ω_μ/ω_p. Even the most unflexible program, GF12, where twelve free parameters are used to fit ten stroboscopic resonances, yields reasonable results. Only the program GF46 yields slightly discrepant results, as do other programs with excessive numbers of free parameters.

We give most weight to program GF22, because it incorporates the effect of the detection-efficiency modulation by incoming muons explicitly, while SF40 and GF31 are only able to adjust a multitude of free parameters whereby the detection-efficiency modulation is absorbed into phenomenological changes of gate lengths.

Finally, we obtain the following results:

$$\begin{aligned} \omega_\mu/\omega_p &= 3.183\,334\,1(19)\,, \quad \text{MuHO in } Br_2\,; \\ \omega_\mu/\omega_p &= 3.183\,321\,2(20)\,, \quad \text{MuBr in } Br_2\,; \\ \omega_\mu/\omega_p &= 3.183\,351\,9(66)\,, \quad \text{MuHO in } H_2O\,. \end{aligned} \tag{4.6}$$

The latter result was obtained by analyzing the data by SF40 only. It will be used for a discussion of chemical reactions of muons in liquids, but not for the final evaluation of μ_μ/μ_p.

These frequencies will have to be corrected for the field shieldings that the muon and proton undergo in their respective probe as well as for the effect of stroboscopic background.

V. CHEMISTRY OF POSITIVE MUONS IN LIQUID BROMINE AND THEIR DIAMAGNETIC SHIELDING (CHEMICAL SHIFT)

A. Introduction

The most critical systematic uncertainty in determining the ratio μ_μ/μ_p is related to the diamagnetic shielding (or chemical shift) of the positive muon in its final chemical environment. There are two questions to be answered. The first one concerns the final chemical situation of the positive muon in the target, the second one is then related to the chemical shift in this particular situation.

As it is hopeless to calculate the absolute value of the chemical shift with the desired precision, one has to choose a target material in which the μ^+ forms a compound the chemical shift of which can be determined accurately by NMR measurements on protons in the analogous molecule. Since from a chemical point of view the positive muon is just a light isotope of the proton, it can be presumed that the muon substituted compound is chemically equivalent to the compound containing the proton. Therefore almost the same diamagnetic shielding for both particles, for muon and proton, can be expected.

However, there will be a small difference due to the different masses of the two particles ($m_\mu \approx \frac{1}{9} m_p$). Different masses will first lead to different zero-point vibration amplitudes, which will result in slightly different bond lengths. Second, the electrons involved in forming the chemical bonds will have slightly different reduced masses, which can affect the electronic structure of the compound as a whole. These isotopic effects on the diamagnetic shielding will however be small, and can be treated by perturbation calculations, while the bulk of the chemical shift is taken from a NMR measurement on the proton-containing compound.

In this spirit, Breskman and Kanofsky[18] have calculated the isotopic effect on the diamagnetic shielding of the "hydrogen nucleus" in a number of diatomic halide molecules in the gas phase. These calculations motivated us to use bromine as target material. Liquid bromine was used in this experiment for two reasons: first, because of its very high stopping power, second, because only in liquid bromine is the density high enough to ensure that muons will undergo chemical reactions in a time period short compared to the muon life time. However, in the liquid phase an additional problem arises from the so-called liquid-association shift and its isotopic-mass dependence.

Experimentally it will turn out that the relevant liquid-association shifts in Br_2 are relatively small (1–2 ppm), in contrast to the situation in water, where the liquid-association shift of protons amounts to +4.58 ppm.[19] In the latter case hydrogen bonding is known to influence the liquid-association shift considerably, while hydrogen bonding is absent in the first case. Since hydrogen bonding should depend on the hydrogen mass (again via zero-point vibration), it is conceivable that the liquid-association shift also displays a significant isotopic-mass dependence. In the absence of such a mechanism, the isotopic-mass depend-

ence of the liquid-association shift can be expected to be small. This is indeed indicated by the outcome of calculations to be discussed in Sec. V D. The stopping targets were prepared from high-purity-grade liquid bromine which was obtained from Merck. After filling the target ampoule, the bromine contained about 0.5 mol% of water. This had an important effect on the final chemical situation of the μ^+. To obtain water-free samples, P_2O_5 was added and, in addition, gaseous HBr was bubbled through, which removed any residual water content by the reaction $HBr + H_2O \rightarrow (H_3O)^+ + Br^-$.

B. The chemistry of μ^+ in liquid Br_2

In the final stage of the slowing down of positive muons in matter, the atom muonium ($Mu = \mu^+ e^-$) is formed,[15] which is the analog to atomic hydrogen (pe^-). While still at epithermal energies, muonium can participate in hot atom reactions, by way of which the μ^+ can be transferred to a different compound (e.g., in water, MuHO is formed[15]), or it gets thermalized as it is. Thermal muonium is expected to react in just the same manner as atomic hydrogen. This has been demonstrated in number of μSR experiments on muonium chemistry.[20,21] In liquid bromine, muons become thermalized very probably as muonium, since the collision partners are heavy. The reaction of H with Br_2 in water as solvent is known to proceed very rapidly as follows:

$$H + Br_2 \xrightarrow[k_H]{} HBr + Br \tag{5.1}$$

with a reaction constant $k_H \approx 10^{11}\,\mathrm{l\,mol^{-1}\,sec^{-1}}$ (Ref. 22).

The analogous reaction for Mu is

$$Mu + Br_2 \xrightarrow[k_{Mu}]{} MuBr + Br\,. \tag{5.2}$$

The corresponding reaction constant has been measured in the solvent C_6H_6 and was found to be $k_{Mu} \approx 10^{11}$ l mol^{-1} sec^{-1} too. This is a typical value for a diffusion controlled reaction rate. It is expected to be the same in liquid Br_2 as well. Consequently, the muon is transferred from Mu to MuBr within an average time of $\tau \approx (k_{Mu} \times [Br_2])^{-1} \simeq 5 \times 10^{-13}$ sec.

If water is present in the sample, MuBr can react further in analogy to the reaction

$$HBr + H_2O \rightarrow (H_3O)^+ + Br^-\,, \tag{5.3}$$

i.e.,

$$MuBr + H_2O \rightarrow (MuH_2O)^+ + Br^-\,. \tag{5.4}$$

The hydronium ion itself will react with water according to

$$(H_3O)^+ + H_2O \rightarrow H_2O + (H_3O)^+ \tag{5.5}$$

or

$$(MuH_2O)^+ + H_2O \rightarrow MuHO + (H_3O)^+\,, \tag{5.6}$$

placing the muon finally into a water molecule. Both reactions (5.3) and (5.5) are proton-transfer reactions; their rates are limited by diffusion only, i.e., by the probability of encounters. The elementary reaction step is thought to proceed by quantum-mechanical tunneling.[23,24] The kinetic rate constants will therefore assume values in the range[23] $k \approx 10^{10}$–10^{11} l mol^{-1} sec^{-1}. Given a water concentration of $H_2O = 0.5$ mol% $= 0.1$ mol l^{-1} the muon will be placed into the water molecule in about $\tau = 2/(k \times [H_2O]) \approx 2(10^{-9} - 10^{-10})$ sec after thermalization.

In a purified Br_2 sample, which will contain some excess HBr from the purification, the reaction $Mu + HBr \rightarrow MuH + Br$ is possible. However, the relevant rate constant is about four orders of magnitude[20] and the HBr concentration about two orders of magnitude smaller than the corresponding values for the process $Mu + Br_2$. Therefore a possible MuH fraction will be negligibly small. It should be mentioned that $(MuH_2O)^+$ does not react with Br_2. In all instances the muon has entered into its final chemical compound in 2 nsec or less. This time is negligibly short compared to the muon lifetime of 2.2 μs.

Furthermore, only one chemical species containing the muon is formed in each of the two different liquid Br_2 samples, namely MuBr in purified bromine and MuHO in bromine contaminated with H_2O. Only the chemical shifts in these two compounds will have to be considered in the further discussion.

C. NMR measurements on the chemical shift of protons in H_2O and HBr in a liquid Br_2 environment

NMR measurements were performed by using a high-resolution NMR spectrometer (Varian A60) operated at room temperature (25 °C). The water contamination of the sample had been detected when the chemical shift of protons was measured as a function of HBr concentration in the liquid Br_2 sample. The proton signal never disappeared, even in nominal zero HBr concentration. It was identified as originating from the H_2O contamination. On the other hand, the proton signal disappeared on adding P_2O_5 to the liquid bromine.

The diamagnetic shielding of protons in H_2O-contaminated liquid bromine was measured in the sample as obtained. The diamagnetic shielding of protons in HBr in liquid Br_2 was measured by first removing the water contamination by adding

TABLE V. Chemical shifts and liquid-association shifts of protons in HBr and H_2O in liquid bromine from proton NMR frequency measurements.

Shift \ $(X)_{Br_2}$	$(HBr)_{Br_2}$	$(H_2O)_{Br_2}$
Measured chemical shift		
$\bar{\sigma}_X - \bar{\sigma}_{water}$ (cylindrical probes)	6.55 ppm[a]	2.40 ppm[a]
Correction for probe shape		
$\frac{2\pi}{3}\chi_v$ (liquid Br_2)[b]	−2.16 ppm	−2.16 ppm
$\frac{2\pi}{3}\chi_v$ (water)[b]	−1.53 ppm	−1.53 ppm
Corrected chemical shift		
$\sigma_X - \sigma_{water}$ (spherical probes)	7.18 ppm	3.03 ppm
Liquid-association shift		
$\sigma_{(X)_{Br_2}} - \sigma_{X_c}$ gas phase,	−1.92 ppm	−1.18 ppm

[a] Typical error: ±0.05 ppm.
[b] From *Eigenschaften der Materie in ihren Aggregatzustanden,* edited by K. H. Hellwege and A. M. Hellwege, *Landolt-Börnstein* (Springer, Berlin, 1967), Vol. 2. Pt. 10.
[c] From Ref. 19.

P_2O_5 and then dissolving gaseous HBr. All measurements were done using long cylindrical NMR probes oriented perpendicularly to the applied field. This geometry implies a shift in the observed resonance frequencies due to a nonzero demagnetization field of $-(2\pi/3)\chi_v B_{ext}$ and the Lorentz field of $+(4\pi/3)\chi_v B_{ext}$, where χ_v is the magnetic bulk susceptibility (emu/cm^3). The total field shift—including the chemical shift σ—is therefore

$$\left(-\sigma + \frac{2\pi}{3}\chi_v\right)B_{ext} = -\bar{\sigma}B_{ext} . \tag{5.7}$$

All shifts were measured relatively to the NMR frequency of protons in pure water. The results are collected in Table V. By comparison with the gas-phase values for HBr and H_2O (Ref. 19), one obtains the liquid-association shifts (last line of Table V). Their values are quite small.

D. Theoretical calculations of the isotope effect on the chemical shift and the liquid-association shift

Breskman and Kanofsky[18] and Williams[25] have considered the isotope effect on the chemical shift in free hydrogen halide molecules by expanding the chemical shift in a Taylor series:

$$\begin{aligned}\Delta\sigma_{\mu\text{-}p} &= \sigma_\mu - \sigma_p \\ &= \sigma'(R_e)[\langle(R-R_e)_\mu\rangle - \langle(R-R_e)_p\rangle] \\ &\quad + \tfrac{1}{2}\sigma''(R_e)[\langle(R-R_e)_\mu{}^2\rangle - \langle(R-R_e)_p{}^2\rangle] + \cdots .\end{aligned} \tag{5.8}$$

$\langle(R-R_e)_{\mu,p}\rangle$ is the average deviation of the muon (or proton) from the equilibrium distance R_e at which the interatomic potential assumes its minimum. If the interatomic potential $V(R)$ is approximated by an anharmonic potential

$$V(R) = V(R_e) + f(R-R_e)^2 - g(R-R_e)^3 , \tag{5.9}$$

one obtains[25]

$$\langle(R-R_e)\rangle = \tfrac{3}{8}\sqrt{2}\,g\hbar\mu^{-1/2}f^{-3/2} , \tag{5.10}$$

where μ is the proton or muon reduced mass. The first derivative of σ, i.e., σ', can be obtained using formulas given by Fixman.[26] The parameters f and g were obtained in Ref. 18 by approximating $V(R)$ by the Morse potential and using the corresponding parameters for the molecules considered. In doing so, Breskman and Kanofsky also demonstrated that the second term in the series Eq. (5.8) can safely be neglected.

The result for $\Delta\sigma_{\mu\text{-}p}$, i.e., the isotopic change of σ in going from HBr to MuBr, is −0.70 ppm,[25] with $\sigma' = 13.0$ ppm/a.u. This result suffers from two—possibly not serious—shortcomings. First, it applies to the free molecule case only, while all the measurements were done in a liquid environment. Second, it is assumed that the interatomic potential does not change with the "hydrogen" mass, i.e., the electronic structure of the molecule is kept fixed.

A recent calculation from first principles by Keller *et al.*[27,28] went beyond these limitations. A cellular multiple-scattering technique and an electron-gas statistical exchange and correlation theory for constructing local one-electron potentials were used to calculate eigenvalues of occupied states, charge densities and potential energy curves as a function of internuclear distance for free HBr and H_2O. The liquid-bromine environment was then taken into account by introducing a boundary potential simulating a shell of Br_2 neighbors. The boundary potential was obtained by smearing out a solvation layer of Br_2 molecules around the molecule under investigation. The liquid was assumed to be close-packed with a local density equal to the average density of liquid bromine.

The change of the intermolecular potential with the isotopic mass of H or Mu, respectively, was—in the case of MuBr—incorporated by solving the Schrödinger equation in the muon cell by the proper use of the e^--p or e^--μ^+ reduced mass. For H_2O/

TABLE VI. Results of the cellular multiple-scattering calculations for molecular HBr and MuBr, and the known experimental values for HBr.

	Free HBr Expt.	Free HBr Calc.	Free MuBr Calc. ($m_e=m_0$)	Free MuBr Calc. ($m_e=m_{red}$)	HBr in liquid Br_2 Calc.	MuBr in liquid Br_2 Calc. ($m_e=m_0$)
Equilibrium distance R_e (a.u.)	2.670	3.053	3.053	3.055	3.190	3.190
Vibrational energy $\frac{1}{2}\hbar\omega_0$ (cm^{-1})	2449	2128	6289	6395	8331	
$E_{binding}+\frac{1}{2}\hbar\omega_0$ (kcal/mol)	86.1	33.9				
$\langle(R-R_e)\rangle$ (a.u.)		0.0249	0.0738		0.0292	0.0865
$\sigma'(R_e)=\frac{\partial\sigma}{\partial R_{H\text{-}Br}}$ (ppm/a.u.)	−13.0[a]		(−8.0),[b] −13.7[b]			
$\Delta\sigma_{isotope}=\sigma_\mu-\sigma_p$ (ppm)			−0.67	−0.70	−0.78	
Liquid association $\Delta\sigma_{liq\ assoc}$ (ppm)	−1.92 (in liq. Br_2)				−1.93	−2.05

[a] From Ref. 18.
[b] Correction discussed in the text.

MuHO the free-electron mass was used throughout.

The intermolecular potentials thus obtained were then used to derive the constants g and f by fitting Eq. (5.9) to the results of the calculation. In the case of H_2O the dependence on the angle between the O-H bonds had to be considered too. This dependence was approximated by

$$V(\theta)=V(\theta_e)+f_\theta(\theta-\theta_e)^2 . \tag{5.11}$$

The isotopic change in the chemical shift was then calculated according to Eq. (5.8).

The liquid-association shift followed from the series expansion (liquid $=l$, gas $=g$):

$$\Delta\sigma_{liq\ assoc}=\sigma_l-\sigma_g=[R_{e,l}-R_{e,g}+\langle(R-R_e)_l\rangle - \langle(R-R_e)_g\rangle]\sigma'(R_e) , \tag{5.12}$$

$\sigma'(R_e)$ was obtained directly by use of Ramsey's formalism.[29] Results are presented in Tables VI and VII. Whenever possible, calculated quantities are compared with experimental values. In the case of HBr it is seen that the bond length is overestimated by a factor of 1.14. It can be shown[27] that $\sigma'(R_e)$ is proportional to R_e^{-4}. Consequently,

TABLE VII. Results of the cellular multiple-scattering calculations for molecular H_2O and MuHO, and the known experimental values for H_2O.

	Free H_2O Expt.	Free H_2O Calc.	Free MuHO Calc.	H_2O in liquid Br_2 Calc.	MuHO in liquid Br_2 Calc.
Equilibrium distance $R_{O\text{-}H}$ (a.u.)	1.809	1.775	1.775	1.835	1.835
Equilibrium angle $\theta_{H\text{-}O\text{-}H}$ (deg.)	104.5	102.3		101.0	
Vibrational energy $\frac{1}{2}\hbar\omega_0$ (cm^{-1})	4628	4475			
$\Delta E_{binding}$ (kcal/mol)	−219.3	−219.6			
$\langle(R-R_e)\rangle$ (a.u.)		0.0124	0.0360	0.0051	0.0148
$\sigma'_{O\text{-}H}=\frac{\partial\sigma}{\partial R_{O\text{-}H}}$ (ppm/a.u.)		(−18.2),[a] −19.6[a]			
$\sigma'_{H\text{-}H}=\frac{\partial\sigma}{\partial R_{H\text{-}H}}$ (ppm/a.u.)		(−2.0)			
$\Delta\sigma_{isotope}=\sigma_\mu-\sigma_p$ (ppm)		−0.46		−0.19	
Liquid association $\Delta\sigma_{liq\ assoc}$ (ppm)	−1.18 (in liq. Br_2)			−1.03	−0.76

[a] Correction discussed in the text.

TABLE VIII. Isotopic changes of the chemical shift and total diamagnetic shielding corrections for the μ^+ in a MuBr or MuHO molecule in liquid Br_2 (spherical probes), absolute and relative to protons in water.

Molecule X + environment	$\Delta\sigma_{\text{isotope}} = \sigma_\mu - \sigma_p$ (ppm) Free molecule	Molecule in liquid	Shielding correction in the liquids $\sigma_X - \sigma_{H_2O}$ (ppm)	σ_X (ppm)
$(MuBr)_{Br_2}$	$-0.70 \pm 15\%$	$-0.78 \pm 15\%$	$+6.40 \pm 0.12$	$+32.04 \pm 0.12$
$(MuHO)_{Br_2}$	$-0.46^{+15\%}_{-110\%}$	$-0.19^{+15\%}_{-110\%}$ $= -0.28 \pm 0.12$	$+2.75 \pm 0.13$	$+28.39 \pm 0.13$
$(MuHO)_{H_2O}$[a]	-2.0 ± 2.0[a]	-2.0 ± 2.0[a]	-2.0 ± 2.0[a]	$+23.64 \pm 2.00$[a]

[a]Values as assumed in Ref. 2 (only for comparison).

the calculated value of $\sigma'(R_e)$, -8.0 ppm/a.u., was corrected by the factor $(3.053/2.670)^4$. The result of -13.7 ppm/a.u. compares very well with the semiempirical value of Ref. 18 and was used in the further procedure.

The heuristic approximation of using the $e^- - \mu^+$ reduced mass affects the isotopic change of the chemical shift by less then 5%. In the calculations on H_2O the electron mass was kept equal to the free-electron mass.

The cellular multiple-scattering calculation in H_2O was improved over the one in HBr in that the cell radii were optimized in a somewhat different fashion.[28] As a result, the equilibrium distance $R_{O\text{-}H}$, the equilibrium bond angle $\theta_{H\text{-}O\text{-}H}$, the vibrational energy, and the binding energy are extremely well reproduced by the calculations. As in the case of HBr, the directly calculated $\sigma'_{O\text{-}H}$ was corrected by $(R_e^{\text{exp}}/R_e^{\text{calc}})^4$, a correction which amounts to less then 8%. As can be seen from Table VII, only the change of the O-H bond length contributes significantly to the change of the chemical shift, while the change of the H-H distance or the bond angle can be neglected ($\sigma'_{H\text{-}H}/\sigma'_{O\text{-}H} \approx 10\%$).

Comparison of the calculated and measured liquid-association shifts of the proton in $(HBr)_{Br_2}$ and $(H_2O)_{Br_2}$ shows a striking agreement. This fact demonstrates the capability of the theoretical methods employed to calculate with high confidence changes of the diamagnetic shielding due to the chemical environment. The authors of Refs. 27 and 28 estimate the following accuracy for the theoretical results: the corrected σ' values carry an uncertainty of $\pm 10\%$, $\langle (R - R_e)_{HBr} \rangle$ carries one of $\pm 5\%$, and $\langle (R - R_e)_{H_2O} \rangle$ carries one of $+100\%$, -5%. The asymmetric uncertainty on the latter quantity is deduced from a consideration of the maximum changes of experimental parameters which allows a reproduction of the vibrational properties of H_2O.

Table VIII lists the isotopic changes of the chemical shift in the gas phase and in the liquid Br_2 environment and gives the corrected values for the difference of the chemical shift of the μ^+ in MuBr/MuHO in liquid Br_2 and for protons in water. The errors on the calculations are added linearly, as well as a 0.05 ppm contribution arising from the NMR measurements. Also shown is the isotopic shift of MuHO in H_2O as given in Ref. 2.

VI. RESULTS AND DISCUSSION

The results given in Eqs. (4.6) have to be corrected for the diamagnetic shieldings of muons in the corresponding molecules. From the discussion of the chemical reactions we arrived at the conclusion that the muon should experience chemical shifts σ_χ as listed in Table VIII. Table IX shows a comparison between predicted and measured differences in the diamagnetic shieldings. Their excellent consistency supports the assumption that hydrogen and muonium chemistry are similar and that the final chemical state of muons stopped in liquid bromine is known. In particular, the difference in diamagnetic shielding of MuHO and MuBr in bromine is accurately reproduced, which strengthens the claim that even secondary chemical reactions are well understood. However, because of the larger uncertainty in the estimation of the chemical shift of MuHO in water (± 2 ppm), we do not use the data from that probe for the determination of μ_μ/μ_p.

The proton spin resonance frequency ω_p has also to be corrected; a value of $\sigma_{NMR} = 25.28(16)$ ppm was derived in Sec. III C 3 on account of the NMR probe calibration. Finally, a correction of

TABLE IX. Predicted and measured differences (in ppm) in the diamagnetic shieldings of $(MuBr)_{Br_2} = A$, $(MuHO)_{BR_2} = B$, and $(MuHO)_{H_2O} = C$.

	Calc.	Expt.
$\sigma_B - \sigma_A$	$-3.65(18)$	$-4.05(87)$
$\sigma_C - \sigma_A$	$-8.4(2.0)$	$-9.6(2.2)$
$\sigma_C - \sigma_B$	$-4.8(2.0)$	$-5.6(2.2)$

TABLE X. Contributions to the final error in μ_μ/μ_p (in ppm)

	$(MuBr)_{Br_2}$		$(MuHO)_{Br_2}$
Statistics (including magnetic-field instability)	0.62		0.59
Chemical shift	0.12		0.13
Combined error	0.64		0.61
Targets combined		0.43	
NMR calibration		0.16	
Spatial field inhomogeneity		0.08	
Stroboscopic background		0.25	
Final error		0.53	

$\sigma_{BG} = -0.20(25)$ ppm has to be applied to ω_p, because of the stroboscopic background.

Thus, by use of Eq. (2.9), yielding

$$\frac{\mu_\mu}{\mu_p} = \frac{\omega_\mu}{\omega_p}\frac{(1+\sigma_X)}{(1+\sigma_{NMR}+\sigma_{BG})}, \tag{6.1}$$

the following results are obtained:

$$\begin{aligned}
&\mu_\mu/\mu_p = 3.183\,343\,4(20), \ 0.6 \text{ ppm}, \ \text{MuBr in } Br_2,\\
&\mu_\mu/\mu_p = 3.183\,344\,7(19), \ 0.6 \text{ ppm}, \ \text{MuHO in } Br_2,\\
&\mu_\mu/\mu_p = 3.183\,344\,1(14), \ 0.4 \text{ ppm}, \ \text{average}.
\end{aligned} \tag{6.2}$$

The errors contain statistical and systematic errors, but not the ones common to both data sets. These are added quadratically to the average value. They include the error in the absolute calibration of the NMR frequency, the error due to the unknown muon-stop distribution and the error attributed to the stroboscopic background. The various error contributions are listed in Table X.

The final result is then obtained,

$$\mu_\mu/\mu_p = 3.183\,344\,1(17), \ \text{i.e., } \pm 0.5 \text{ ppm}. \tag{6.3}$$

This value can be compared with other values of μ_μ/μ_p which are listed in Table XI. All values are in good agreement with each other.

A precise value of μ_μ/μ_p is needed to determine the following quantities.

(*a*) *The anomaly of the muonic magnetic moment.* In the CERN muon storage-ring experiment, the anomalous part of the muonic magnetic moment was measured and a result of

$$\mu_a/\mu_p = 0.003\,707\,213(27)$$

was obtained.[5] μ_μ/μ_p and μ_a/μ_p yield the muonic magnetic-moment anomaly

$$a_\mu(\text{expt}) = \frac{\mu_a/\mu_p}{\mu_\mu/\mu_p - \mu_a/\mu_p} = 0.001\,165\,923\,0(85). \tag{6.4}$$

This value is practically unchanged when compared to the value given in Ref. 5.

The current theoretical result[30] is $a_\mu(\text{theory}) = 0.001\,165\,921\,3(98)$. The agreement between theory and experiment is excellent.

(*b*) *The muon mass.* The muonic magnetic moment and muon mass are related by

$$m_\mu/m_e = (g_\mu/2)(\mu_\mu/\mu_p)^{-1}\mu_B/\mu_p.$$

Thus we obtain

$$m_\mu/m_e = 206.768\,35(11) \tag{6.5}$$

by taking for the muon g factor

$$g_\mu = 2(1+a_\mu) = 2\times 1.001\,165\,923\,0(85),$$

and for the proton magnetic moment in units of the Bohr magneton $\mu_p/\mu_B = 0.001\,521\,032\,209(16)$.[31]

(*c*) *The hyperfine structure interval of muonium*

TABLE XI. Experimental values of μ_μ/μ_p (1971–1981).[a]

Method	Magnetic field	μ_μ/μ_p	Ref.
Precession in water	1.10 T	3.183 346 7(82)	2
Muonium HFS	0	3.183 343 6(44)[b]	4
Muonium HFS	1.36 T	3.183 340 3(44)	9
Muonium HFS	1.36 T	3.183 344 1(43)[b]	9
Precession in bromine	0.75 T	3.183 344 1(17)[c]	Present work

[a] *Note added in proof.* A preliminary evaluation of newer data obtained by the measurement of the hyperfine structure transitions in muonium at 1.36 T yielded the result $\mu_\mu/\mu_p = 3.183\,344\,78(96)$, in excellent agreement with our Quantum value. Quoted from H. Orth, in *Present Status and Aims of Electrodynamics* (Ref. 30).

[b] These values are (re)calculated from the HFS of muonium by use of Eq. (6.6). In Ref. 4 a value of 3.183 329 9(25) was given which was based on an incorrect theoretical expression for ν_{HFS}.

[c] The present value supersedes $\mu_\mu/\mu_p = 3.183\,344\,8(29)$ published in Ref. 1.

Using[31]

$$\alpha^{-1} = 137.035\,963(15)\,,$$

$$c = 2.997\,924\,580(12) \times 10^{10}\ \text{cm/sec}\,,$$

$$R_\infty = 109\,737.314\,76(32)\ \text{cm}^{-1}\,,$$

the theoretical value for the hyperfine structure interval of muonium can be calculated,[32]

$$\nu_{\text{HFS}}(\text{theory}) = \tfrac{16}{3}\alpha^2 R_\infty (\mu_\mu/\mu_p)(\mu_p/\mu_B)(1+m_e/m_\mu)^{-3} \times (1+\tfrac{3}{2}\alpha^2 + a_e + \epsilon_1 + \epsilon_2 + \epsilon_3 - \delta_\mu + \text{higher-order terms}) \quad (6.6)$$

with

$$a_e = \frac{\alpha}{2\pi} - 0.328\,478\,97\frac{\alpha^2}{\pi^2} + 1.1835(61)\frac{\alpha^3}{\pi^3}\,,$$

$$\epsilon_1 = \alpha^2(\ln 2 - \tfrac{5}{2})\,,$$

$$\epsilon_2 = \frac{8\alpha^3}{3\pi}\ln\alpha(\ln 4 - \ln\alpha - \tfrac{281}{480})\,,$$

$$\epsilon_3 = \frac{\alpha^3}{\pi}(18.4 \pm 5)\,,$$

$$\delta_\mu = \frac{m_e}{m_\mu}\left[\frac{3\alpha}{\pi}\frac{m_\mu^2}{m_\mu^2 - m_e^2}\ln m_\mu/m_e - 2\alpha^2\ln(1/\alpha)(1+m_e/m_\mu)^{-2} + 2\frac{\alpha^2}{\pi^2}(\ln m_\mu/m_e)^2\right].$$

The evaluation yields

$$\nu_{\text{HFS}}(\text{theory}) = 4\,463\,302.86\ \text{kHz}\,. \quad (6.7)$$

There are several contributions to the error in this value. (i) The error in ϵ_3 contributes 2.8 kHz. (ii) There are two uncalculated contributions to the recoil corrections δ_μ which are usually written in the form[32]

$$D\frac{m_e}{m_\mu}\frac{\alpha^2}{\pi^2}\ln\frac{m_\mu}{m_e} + E\frac{m_e}{m_\mu}\alpha^2 = (0.14D + 0.26E)\ \text{ppm} \approx 4.0\ \text{kHz}\,.$$

(iii) The uncertainty in α contributes 1.0 kHz. (iv) The error in μ_μ/μ_p contributes 2.4 kHz. (v) All other fundamental quantities contribute 0.4 kHz. It seems safe to ascribe a total error of 6 kHz to $\nu_{\text{HFS}}(\text{theory})$. In any case the agreement with experimental value[9]

$$\nu_{\text{HFS}}(\text{expt}) = 4\,463\,302.35(52)\ \text{kHz}\,.$$

is excellent. The capability of quantum electrodynamics and particularly of the Bethe-Salpeter equation to describe with high precision relativistic two-body bound states is therefore again successfully demonstrated.

ACKNOWLEDGMENTS

We would like to express our thanks to Professor W. Känzig for the loan of the Varian magnet, and Dr. K. Borer and Dr. F. Lange for their advice on construction and calibration of the NMR probes. We are endebted to Dr. Mathiasch for his help in the NMR measurements, and to Professor H. Fischer for enlightening discussions on the chemical processes involved. We appreciate the contributions of Dr. B. D. Patterson in the early stage of the experiment, and the helpful cooperation of the SIN accelerator crew. We also would like to thank Professor H.-J. Gerber and Dr. G. H. Eaton for the careful reading of the manuscript.

This work was supported by the Bundesministerium für Forschung und Technologie of the Federal Republic of Germany and by the Schweizerisches Institut für Nuklearforschung (SIN).

APPENDIX

The number of counts N_j in one of the stroboscopic gates $G_j(t)$ was shown to be given by Eq. (2.4),

$$N_j = D\int_0^\infty dt'\frac{1}{\tau_\mu}e^{-t'/\tau_\mu}[1 + A\cos(\omega_\mu t' - \Phi)] \times \int_{t_i}^{t_f} dt\, B(t-t')G_j(t)\,. \quad (A1)$$

Here we will derive the shape of the stroboscopic resonance, i.e., the number of positrons counted in one of the gates $G_j(t)$, as a function of the external magnetic field, or equivalently, as a function of the μ^+ spin-precession frequency ω_μ.

We define

$$S_j(t') = \frac{1}{t_f - t_i}\int_{t_i}^{t_f} B(t-t')G(t)dt\,, \quad (A2)$$

which we call the stroboscopic structure function. It contains all the specific features of a measurement, like structural influences due to the particular beam-burst shape and to the electronic gates, as well as transient features due to singular distortions. As one expects, it can be shown that the transient features vanish in the limit of a large data-taking time interval $(t_f - t_i)$ and that only the periodic features survive.

The muon beam can be described as a superposition of individual bunches of muons, the muon bursts,

$$B(t) = B\sum_{n=-\infty}^{\infty} b(t - nT - t_B)\,. \quad (A3)$$

Here $b(t)$ describes the time structure of an individual burst, t_B defines the time offset of the bursts relative to an arbitrary time-synchroniza-

tion signal periodic with the accelerator frequency $\Omega = 2\pi/T$. If $b(t)$ is normalized by $\int_{-\infty}^{\infty} b(t)dt = 1$, then B is the average number of stopped muons per burst. $N_0 = DB(t_f - t_i)/T$ is the total number of detected positrons in $(t_f - t_i)$.

The Fourier transform of $b(t)$ is given by

$$\hat{b}(\omega) = \int_{-\infty}^{\infty} b(t)e^{-i\omega t}dt \,. \tag{A4}$$

Taking into consideration the properties of Fourier integrals and Fourier series, we can calculate

$$B(t) = \frac{B}{T}\sum_{m=-\infty}^{\infty} \hat{b}(m\Omega)e^{im\Omega(t-t_B)} \,. \tag{A5}$$

Similarly one has

$$G_j(t) = \sum_{k=-\infty}^{\infty} g_j(t - kT - t_j) \,, \tag{A6}$$

$$\hat{g}_j(\omega) = \int_{-\infty}^{\infty} g_j(t)e^{-i\omega t}dt \,, \tag{A7}$$

$$G_j(t) = \frac{1}{T}\sum_{n=-\infty}^{\infty} \hat{g}_j(n\Omega)e^{in\Omega(t-t_j)} \,, \tag{A8}$$

with obvious notations. The gate function $g_j(t)$ is normalized by $\int_{-\infty}^{\infty} g_j(t)dt = \lambda_j T$, where λ_j is the fractional width of the gate G_j.

One writes now (A2) as

$$S_j(t') = \frac{1}{t_f - t_i}\frac{B}{T}\sum_{m=-\infty}^{\infty} \hat{b}(m\Omega)\frac{1}{T}\sum_{n=-\infty}^{\infty} \hat{g}_j(n\Omega)\int_{t_i}^{t_f} e^{im\Omega(t-t'-t_B)}e^{in\Omega(t-t_j)}dt \,. \tag{A9}$$

In the limit of a long data-taking interval, the integration yields only nonvanishing contributions for $m = -n$,

$$S_j(t') = \frac{B}{T}\sum_{n=-\infty}^{\infty} \frac{1}{T}\hat{b}^*(n\Omega)\hat{g}_j(n\Omega)e^{in\Omega(t'+t_B-t_j)} \,. \tag{A10}$$

The relation $\hat{b}(-n\Omega) = \hat{b}^*(n\Omega)$, satisfied for real functions $b(t)$, has been used.

We define

$$\hat{s}_j(\omega) = \hat{b}^*(\omega)\hat{g}_j(\omega) \,, \tag{A11}$$

which is the Fourier transform of

$$s(t') = \int_{-\infty}^{\infty} dt\, b(t - t')g(t) \,, \tag{A12}$$

and similarly to (A3) or (A6) we have

$$S_j(t') = \frac{B}{T}\sum_{m=-\infty}^{\infty} s_j(t' + t_B - t_j - mT) \,.$$

Thus (A1) takes the form

$$N_j = N_0 \sum_{m=-\infty}^{\infty} \frac{1}{T}\hat{s}_j(m\Omega)e^{im\Omega(t_B-t_j)} \times \int_0^{\infty} dt' \frac{1}{\tau_\mu}e^{-t'/\tau_\mu} \times [1 + A\cos(\omega_\mu t' - \phi)]e^{im\Omega t'} \,. \tag{A13}$$

Using

$$\int_0^{\infty} dt' \frac{1}{\tau_\mu}e^{-t'/\tau_\mu \pm i\omega t'} = \frac{1}{1 \mp i\omega\tau_\mu} \,,$$

one can calculate the integral in (A13), which yields

$$\frac{1}{1 - im\Omega\tau_\mu} + \frac{A}{2}\left(\frac{e^{-i\phi}}{1 - i(m\Omega + \omega_\mu)\tau_\mu} + \frac{e^{i\phi}}{1 - i(m\Omega - \omega_\mu)\tau_\mu}\right) .$$

In the summation over m, m can be replaced by $-m$ for the terms containing $e^{-i\phi}$. Then

$$N_j = N_0\left\{\sum_{m=\infty}^{\infty} \frac{1}{T}\frac{\hat{s}_j(m\Omega)}{1 - im\Omega\tau_\mu}e^{im\Omega(t_B-t_j)} + \frac{A}{2}\sum_{m=-\infty}^{\infty} \frac{1}{T}\left[\frac{\hat{s}_j(-m\Omega)e^{-i\phi-im\Omega(t_B-t_j)}}{1 + i(m\Omega - \omega_\mu)\tau_\mu} + \frac{\hat{s}_j(m\Omega)e^{i\phi+im\Omega(t_B-t_j)}}{1 - i(m\Omega - \omega_\mu)\tau_\mu}\right]\right\} . \tag{A14}$$

The first term represents the unpolarized contribution, which does not depend on the magnetic field. It is dominated by its $m = 0$ component and therefore reduces essentially to $N_0\lambda_j$. The second term exhibits a resonant behavior. Since $\hat{s}(-\omega) = \hat{s}^*(\omega)$, every term of the sum is real and the polarized contribution can be written as

$$N_0 A\frac{1}{T}\sum_{m=-\infty}^{\infty} \mathrm{Re}\left(\frac{\hat{s}_j(m\Omega)e^{i\phi+im\Omega(t_B-t_j)}}{1 + i(\omega_\mu - m\Omega)\tau_\mu}\right) = N_0 A\frac{1}{T}\sum_{m=-\infty}^{\infty} |\hat{s}_j(m\Omega)| \times \frac{\cos\psi_{m,j} - (\omega_\mu - m\Omega)\tau_\mu \sin\psi_{m,j}}{1 + (\omega_\mu - m\Omega)^2\tau_\mu{}^2} \,, \tag{A15}$$

where

$$\psi_{m,j} = m\Omega(t_j - t_B) - \phi - \arg[\hat{s}_j(m\Omega)] \,.$$

The sign convention has been chosen such that the phase $\psi_{m,j}$ increases for successive time gates (for symmetric beam bursts and proper choice of t_B, the coefficients $\hat{s}(m\Omega)$ are real and $\arg[\hat{s}_j(m\Omega)] = 0$).

By defining

$$A_{\mathrm{eff},j}(m\Omega) = A|\hat{b}(m\Omega)|\,|\hat{g}(m\Omega)|/(\lambda_j T) \tag{A16}$$

and $x_m = (\omega_\mu - m\Omega)\tau_\mu$, we arrive at

$$N_j = N_0 \lambda_j \left[1 + \sum_{m=-\infty}^{\infty} A_{\mathrm{eff},j}(m\Omega) \frac{\cos\psi_{m,j} - x_m \sin\psi_{m,j}}{1 + x_m^2} \right] . \tag{A17}$$

For rectangular gates $g_j(t) = \theta(t - \frac{1}{2}\lambda_j T)\theta(\frac{1}{2}\lambda_j T - t)$, where θ is the Heaviside function, the Fourier transform of $g_j(t)$ is given by

$$\hat{g}_j(\omega) = \lambda_j T \sin(\lambda_j \omega T/2)/(\lambda_j \omega T/2) .$$

The muon beam burst can approximately be described by Gaussians,

$$b(t) = (\kappa T \sqrt{\pi})^{-1} \exp[-(t/\kappa T)^2] ,$$

where κ is a measure of the width of the beam bursts. The Fourier transform of $b(t)$ is then

$$\hat{b}(\omega) = \exp[-(\kappa \omega T/2)^2] .$$

For rectangular gates and Gaussian beam bursts the asymmetry yields therefore

$$A_{\mathrm{eff},j}(m\Omega) = A e^{-(m\pi\kappa)^2} \sin(m\pi\lambda_j)/(m\pi\lambda_j) . \tag{A18}$$

---

*Present address: Dipartimento Cantonale dell'Ambiente, CH-6500 Bellinzona, Switzerland.

[1]M. Camani, F. N. Gygax, E. Klempt, W. Rüegg, A. Schenck, H. Schilling, R. Schulze, and H. Wolf, Phys. Lett. 77B, 326 (1978).
[2]K. M. Crowe, J. F. Hague, J. E. Rothberg, A. Schenck, D. L. Williams, R. W. Williams, and K. K. Young, Phys. Rev. D 5, 2145 (1972).
[3]R. De Voe, P. M. McIntyre, A. Magnon, D. Y. Stowell, R. A. Swanson, and V. L. Telegdi, Phys. Rev. Lett. 25, 1779 (1970).
[4]D. E. Casperson, T. W. Crane, V. W. Hughes, P. A. Souder, R. D. Stambaugh, P. A. Thompson, H. Orth, G. zu Putlitz, H. F. Kaspar, H. W. Reist, and A. B. Denison, Phys. Lett. 59B, 397 (1975).
[5]J. Bailey, K. Borer, F. Combley, H. Drumm, C. Eck, F. J. M. Farley, J. H. Field, W. Flegel, P. M. Hattersley, F. Krienen, F. Lange, G. Lebée, E. McMillan, G. Petrucci, E. Picasso, O. Rúnolfsson, W. von Rüden, R. W. Williams, and S. Wojcicki, Nucl. Phys. B150, 1 (1979).
[6]G. Peter Lepage, Phys. Rev. A 16, 863 (1977).
[7]G. T. Bodwin, D. R. Yennie, and M. A. Gregorio, Phys. Rev. Lett. 41, 1088 (1978).
[8]W. E. Caswell and G. Peter Lepage, Phys. Rev. Lett. 41, 1092 (1978).
[9]D. E. Casperson, T. W. Crane, A. B. Denison, P. O. Egan, V. W. Hughes, F. G. Mariam, H. Orth, H. W. Reist, P. A. Souder, R. D. Stambaugh, P. A. Thompson, and G. zu Putlitz, Phys. Rev. Lett. 38, 956 (1977).
[10]J. Christiansen, H. E. Mahnke, E. Recknagel, D. Riegel, G. Schatz, G. Weyer, and W. Witthuhn, Phys. Rev. C 1, 613 (1970).
[11]K. Borer, Nucl. Instrum. Methods 143, 203 (1977).
[12]K. Borer and F. Lange, Nucl. Instrum. Methods 143, 219 (1977).
[13]W. D. Phillips, W. E. Cook, D. Kleppner, Metrologia 13, 179 (1977).
[14]J. C. Hindman, J. Chem. Phys. 44, 4582 (1966).
[15]See, e.g., J. H. Brewer, K. M. Crowe, F. N. Gygax, and A. Schenck, in *Muon Physics*, edited by V. W. Hughes and C. S. Wu (Academic, New York, 1975), Vol. III, p. 3ff.
[16]F. James and M. Roos, MINUIT, CERN Computer Center Program Library (CERN, Geneva, 1978).
[17]S. Kazama and Y. Fukai, J. Less-Common Metals 54, 25 (1977).
[18]D. Breskman and A. Kanofsky, Phys. Lett. 33B, 309 (1970).
[19]W. G. Schneider, H. J. Bernstein, and J. A. Pople, J. Chem. Phys. 28, 601 (1958).
[20]J. H. Brewer and K. M. Crowe, Annu. Rev. Nucl. Part. Sci. 28, 239 (1978).
[21]P. W. Percival, Radiochim. Acta 26, 1 (1979).
[22]Farhataziz, J. Phys. Chem. 71, 598 (1967).
[23]M. Eigen, Angew. Chem. Int. Ed. Engl. 3, 1 (1964).
[24]E. F. Caldin, Chem. Rev. 69(1), 135 (1969).
[25]R. W. Williams, Phys. Lett. 34B, 63 (1971).
[26]M. Fixman, J. Chem. Phys. 35, 679 (1961).
[27]M. Castro, J. Keller, and A. Schenck, Hyperfine Interact. 6, 439 (1979).
[28]M. Castro and J. Keller, report UNAM, Facultad de Quimica, Mexico City, 1980 (unpublished).
[29]N. F. Ramsey, Phys. Rev. 78, 699 (1950).
[30]See, e.g., E. Borie and J. Calmet, in *Present Status and Aims of Quantum Electrodynamics*, proceedings of the Symposium, Mainz, Germany, 1980, edited by G. G. Gräff, E. Klempt, and G. Werth, *Lecture Notes in Physics 143* (Springer, Berlin, 1981), p. 68.
[31]Values of fundamental constants are taken from a recent compilation of B. N. Taylor, in Particle Data Group, Rev. Mod. Phys. 52, S33 (1980).
[32]See, e.g., T. Kinoshita, in *Proceedings of the 11th International Conference on High Energy Physics, Tokyo, 1978*, edited by S. Homma, M. Kawaguchi, and H. Miyazawa (Phys. Soc. of Japan, Tokyo, 1979), p. 571.